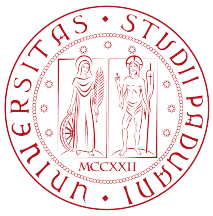

Università degli Studi di Padova
Dipartimento di Fisica ed Astronomia "G. Galilei"

Tesi di Laurea Magistrale in Fisica

Surface temperature distribution and absorption features in Isolated Neutron Stars

Candidata: **Alice Borghese**

Relatore: **Prof. Roberto Turolla**

Correlatore: **Dott.ssa Nanda Rea**
Dott. Daniele Viganò

Anno Accademico 2013/2014

Ai miei nonni Chiara e Rinaldo,
i miei neutrini preferiti

Fare della fisica vuol dire cercare le leggi della natura. E un fisico non è uno strano uomo che parla uno strano linguaggio, chiuso in uno strano tempio; ma è un uomo che ha la fantasia di un poeta, l'abilità manuale di un meccanico e il rigore di un matematico; egli deve ideare le esperienze, costruire gli apparecchi per eseguirle e conoscere le più astruse teorie matematiche per discutere e vagliare i risultati delle sue esperienze. La vita di un fisico è un seguito di eccitanti avventure e un fisico che descrive la propria ricerca è come un compositore che scrive la propria sinfonia.
Ginestra Amaldi

Contents

Preface

Neutron stars are truly fascinating objects. About 10 km in radius, neutron stars have a mass approximately the same as the Sun; their density can reach values of the order of $\sim 10^{14}$ g cm^{-3}. They have huge magnetic fields ranging between 10^{10} - 10^{15} G. Neutron stars are ideal astrophysical laboratories and provide an unique environment with extreme density, temperature, magnetic and gravitational field. They offer connections among nuclear physics, particle physics and astrophysics. Chapter 1 includes an overall description of neutron stars.

In the last decades, thanks to *Chandra* and *XMM-Newton*, several puzzling sub-classes of isolated neutron stars were discovered: Anomalous X-ray Pulsars (AXPs), Soft Gamma Repeaters (SGRs), Rotating Radio Transients (RRATs), X-ray Dim Isolated Neutron stars (XDINSs), and Central Compact Objects (CCOs). The aim is to unify all known classes of sources considering them as different manifestations of the same underlying physics. Hypothesis for grand unification have been proposed, for instance a theory of magneto-thermal evolution may establish the evolutionary links between these different families. According to it thermal evolution and magnetic field decay are inseparable; the basis of this theory and the recent results are described in chapter 2.

This work focuses on the XDINSs, also known as the Magnificent Seven. This group of neutron stars share a number of common properties, such as very low values of the column density, no radio emission, pulsation periods in a restricted range $P \sim$ 3-12 s, and very faint optical counterparts implying an exceedingly large X-ray-to-optical flux ratio. They show only thermal emission with typical temperature in the range $\sim$ 50-100 eV. The characteristics of the Magnificent Seven are reported in chapter 3.

In five of the XDINSs deviations from a pure blackbody spectrum have been detected in form of broad absorption features. Their nature is not clear

yet; they can be understood in the context of proton/electron cyclotron resonances and/or atomic transitions in a magnetised atmosphere. It is almost certain that the star magnetic field plays a fundamental role in their formation; absorption features may provide a powerful mean to estimate the surface field strength. Very recently a new explanation has been suggested [1]: distortions from Planckian spectrum can be induced by inhomogeneous temperature distributions of the neutron star surface. In this work I investigate this hypothesis for four XDINS: RX J2143.0+0654, RX J0720.4-3125, RX J1605.3+3249, and RX J1308.6+2127. For these sources I re-analyse the available *XMM-Newton* data, extracting phase integrated spectra. Then, I consider several simple surface temperature distributions building model spectra in the hypothesis of blackbody emission at local temperature. These analytical model have been finally used to fit *XMM-Newton* spactral data. Results are presented in chapter 4.

Chapter 1

Neutron stars

The existence of neutron stars (NS hereafter) was first proposed by the astrophysicists Walter Baade and Fritz Zwicky: "With all reserve we advance the view that a supernova represents the transition of an ordinary star into a neutron star, consisting mainly of neutrons" [2]. It was 1934, only two years after the discovery of the neutron by J. Chadwick. They were aware that NSs could have peculiar characteristics, in particular small radii and very high densities.

Then, in 1967, Jocelyn Bell, who was doing research in radio astronomy at Cambridge University under the supervision of A. Hewish, detected regular radio pulse from an unknown source with a period of about 1.3 seconds [3]. Several explanations were put forward, including that the signals might be generated by another civilisation, named Little Green Men. However, as other sources were detected, it was clear that a new class of celestial objects was being discovered. They were called 'pulsars', which stands for pulsating radio sources. The link between pulsars and NSs was provided by F. Pacini and other astrophysicists, such as T. Gold [4]. Few months before Bell's discovery the former proposed that the Crab Nebula was powered by a neutron star which was rapidly rotating and highly magnetised [5]. Thanks to Bell's detections, it was possible to identify pulsar with rotating NSs.

NSs are remnants of massive stars, the core of which collapsed in the supernova event. The initial mass of the progenitor establishes which type of compact object is born, NSs are thought to originate from stars with mass in the range $\sim$ 8 - 25 $M_\odot$[1]. Conservation of both the angular momentum and the magnetic flux of the progenitor star during the collapse gives the NS a high spin rate and huge magnetic field. These objects have typical mass M of

[1] $M_\odot = 1.99 \times 10^{33}$ g is the solar mass.

the order of 1 $M_\odot$ and radius R of ~ 10 km. Their density can reach values of the order of $\sim 10^{14}$ g cm^{-3} and increases moving inward: the central density is as high as 5 to 10 times the nuclear equilibrium density $n_0 \cong 0.16$ fm^{-3} of neutrons and protons found in nuclei [6]. Thus, NSs are the densest known objects in the Universe and, as such, are ideal astrophysical laboratories for studying matter under extreme densities and provide connections among nuclear physics, particle physics and astrophysics.

1.1 Formation

A main sequence star, with a central temperature of $\sim 10^7$ K, burns hydrogen nuclei to form helium. When H is spent in the core, He starts to be burnt at $\sim 10^8$ K producing oxygen and carbon. A star of initial mass above 8 $M_\odot$ is able to ignite O and C in order to produce heavier elements, such as neon and silicon. The star internal temperature increases and burning continues until elements of the iron peak are produced. However, thermonuclear fusion of nuclei of the iron group (Fe, Ni, Co) is an endothermic process, therefore it cannot take place in the stellar core. At this stage the core density increases and degenerate electrons are responsible for the pressure which balances the gravitational force. When the core reaches the Chandrasekar limit, it starts to collapse, because the degeneracy pressure can no longer support the star, and its temperature increases till $\sim 10^9$ K. The photondisintegration of ^{56}Fe into ^{4}He is the crucial mechanism which triggers the collapse:

$$^{56}\mathrm{Fe} + \gamma \rightarrow 13\ ^4\mathrm{He} + 4n$$

$$^4\mathrm{He} + \gamma \rightarrow 2p + 2n.$$

These reactions make the core rich in neutrons; when the density is about $\sim 10^7$ g cm^{-3} inverse β-decay, $p+e^- \rightarrow n+\nu_e$, becomes energetically favourable. As a consequence the number of free neutrons grows and their degeneracy pressure balances the gravitational force.

The proto-neutron star consists of neutrons, protons and leptons, mostly e^- and ν_e. Neutrinos play an important role in supernova explosions, since they carry away a great amount of the released energy. The collapse ends when the star central density reaches n_0, this event gives rise to a shock wave which propagates about 100-200 km before it stops, having lost energy to neutrinos. It might be that neutrinos from the core, helped by rotation, convection or magnetic fields, resuscitate the shock; if it happens the stellar mantle is expelled and the newly born neutron stars remains. In about 50 s the neutrino mean free path exceeds the NS dimension, so the compact

object become transparent to νs; because of neutrino cooling, within 10 to 100 years the NS becomes an isothermal structure with temperature of the order of $\sim 10^8$ - 10^9 K (Fig. 1.1). There are two possible mechanisms of neutrino emission [7]:

- direct Urca[2] process, which involve nucleons

$$n \to p + e^- + \overline{\nu}_e$$

$$p \to n + e^+ + \nu_e;$$

  β-decay is allowed if both energy and momentum can be simultaneously conserved. This requires that the proton-to-neutron ratio exceeds 1/8, which is far above the value found in the core. Therefore neutrino production via direct Urca is possible if exotic states are present in the core.

- modified Urca process (MUrca)

$$n + (n, p) \to p + (n, p) + e^- + \overline{\nu}_e$$

$$p + (n, p) \to n + (n, p) + e^+ + \nu_e;$$

  where an additional nucleon is introduced in order to guarantee momentum conservation.

According to the standard cooling scenario, Urca process cannot occur. Since MUrca is less efficient than the direct Urca, the NS cooling proceeds slowly; after $\sim 10^5$ years the photon emission becomes the dominant mechanism to lose energy. Other ingredients that can influence the NS cooling are superfluidity, magnetic fields, and mass accretion. Superfluidity affects the neutrino emissivity and the heat transport from the interior to the outer NS layers. The main effect of the magnetic field is breaking the spherical symmetry in the heat transport; in fact the thermal conductivity becomes anisotropic, developing a surface temperature gradient. The presence of an accreted envelope of light elements in the NS crust can instead enhance the thermal conductivity of the outer layers. The NS should remain observable by surface thermal emission for up to a few million years.

[2]Urca was the name of a casino in Rio de Janeiro. It was chosen as a name for these processes by Gamow and Schoenberg who said that "the energy disappears in the nucleus of the supernova as quickly as the money disappeared at that roulette table".

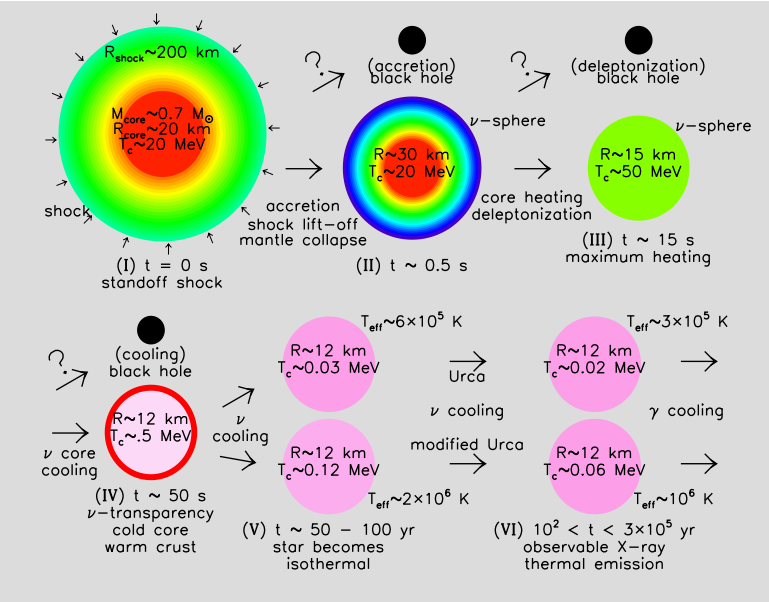

Figure 1.1: The main stages of evolution of a neutron star [6].

1.2 Structure

The global properties of NSs are described by two equations:

$$\frac{dP(r)}{dr} = -\frac{\rho(r)m(r)}{r^2}\left(1+\frac{P(r)}{\rho(r)}\right)\left(1+\frac{4\pi r^3 P(r)}{m(r)}\right)\left(1-\frac{2m(r)}{r}\right)^{-1} \tag{1.1}$$

$$\frac{dm(r)}{dr} = 4\pi r^2 \rho(r), \tag{1.2}$$

where P is the isotropic pressure, ρ is the total mass-energy density, m is the gravitational mass, r is the radial coordinate; we assume $c = 1 = G$.
The first equation is called TOV (Tolman-Oppenheimer-Volkoff) equation, it is derived by solving the Einstein equations for a general time-invariant, spherically symmetric space-time. It is the relativistic version of Newtonian hydrostatic balance (the relativistic corrections are the terms added to one in brackets). The second equation represents the gravitational mass enclosed between a radius r and $r + dr$.

These are two equations in three unknown quantities: $P(r)$, $\rho(r)$ and $m(r)$. Therefore a third equation is required in order to close the system:

the equation of state (EoS) $P = P(\rho)$, if the medium is barotrope. It is determined by the model adopted to describe the matter inside the star. This system of differential equations is solved imposing the boundary conditions $\rho(0) = \rho_c$ and $P(R_\star) = 0$. Once the NS radius $R_\star$ is fixed, the solution provides the star mass $M_\star$, or vice versa. The biggest problem is that the EoS is still an open question in neutron star astrophysics. TOV equation could be used to determine one. In fact, assuming a certain EoS, it is then possible to solve TOV which gives a relation in the mass-radius diagram. A simultaneous measurement of mass and radius of a NS could help to exclude or confirm TOV solutions, consequently to discriminate the correct EoS among the families of possible equations.

Radius can be inferred from observations assuming that all the surface is emitting at the same temperature, so the ideal candidate is an isolated and weakly magnetized NS. The NS needs to be isolated, otherwise the accretion disk emits; a weak magnetic field does not make the conductivity too much anisotropic, so the temperature could be considered constant on the whole surface. There are some binary systems, known as soft x-ray transients, where the NS orbits a Be star in a very eccentric orbit, accreting material only occasionally when the NS crosses a disk of material surrounding the Be star. Far from the companion, accretion stops and the NS cools and is weakly magnetized. These systems have been used to make radius measurements [8]. The most reliable way of determining astronomical masses is via Kepler's third law, therefore it is necessary to use a binary system, where at least one of star spectra can be detected. From Kepler's law we can obtain the mass function which depends on observable quantities, such as the period of the orbit and the projection of orbital velocity. If only one mass function can be measured, we have a lower limit for the mass of the object with unknown spectrum. Moreover, a NS cannot be more massive than $\sim 3\ M_\odot$, a limit set by causality [9] the speed of sound in dense matter is less than the speed of light. The minimum stable NS mass is about $0.1\ M_\odot$, although a more realistic minimum stems from the NS origin acting in a supernova explosion [6]. The most accurately measured NS masses are from timing observations of binary radio pulsars [10]. A measurement of the gravitational red-shift at the surface of a NS provides a direct constraint on the mass-to-radius ratio. This requires the presence of some spectral features; they are red-shifted according to the formula

$$\lambda_\infty = \lambda \left(1 - \frac{2GM_\star}{R_\star c^2}\right)^{-1}$$

where λ_∞ is the wavelength measured by the observer and λ is the one measured in the laboratory. If λ is known, $M_\star/R_\star$ can be deduced.

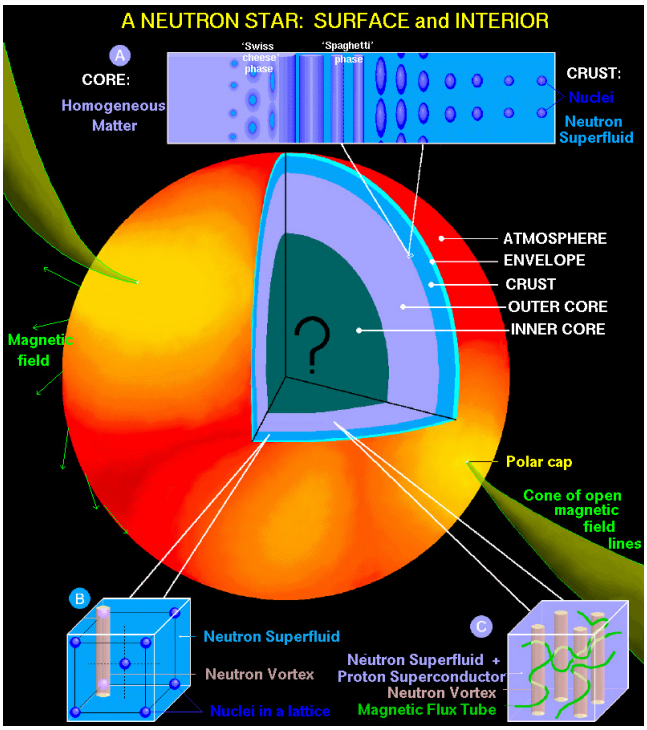

Figure 1.2: The internal structure of a NS [6].

The internal structure of a NS is depicted in figure 1.2. The outermost layers (few cm to $\sim$ 100 m) are called atmosphere and envelope (or ocean); they contain a negligible amount of mass. In the atmosphere the thermal radiation is released and its chemical composition is thought to leave an imprint on the observed spectra. The envelope has a low density ($\rho \lesssim 10^9$ g cm^{-3}) and it is where the largest gradients of temperature, density and pressure are reached. The transition between atmosphere and ocean occurs where the nuclei become a liquid. Further in, the matter becomes solid and a new layer, the crust, develops extending about 1 to 2 km. It is made of a Coulomb lattice of nuclei and a free gas of ultra-relativistic degenerate electrons; the neutron drip density $\rho_d \sim 10^{11}$ g cm^{-3} defines the boundary between the outer and the inner crust. In the latter it is energetically favourable for neutrons to float out of nuclei and move freely; at the highest densities in the crust, nearly all the mass resides in the neutron fluid than in the nuclei.

Close to the crust/core interface, the spherical shape of nuclei is not energetically favoured due to the high energy cost required by Coulomb repulsion, so continuous changes in dimensionality of matter occur [11]. These phases are collectively named nuclear pasta, by analogy to the shape of spaghetti,

lasagne and maccheroni and they represent the transition to the core. With density $\rho \sim 10^{14}$ g cm^{-3} and radius of ~ 10 km, the core constitutes up to 99% of the mass of the star. The outer core is made of nucleons, electrons and muons; in the inner core exotic particles such as strangeness-bearing hyperons, Bose condensates (pions or kaons) and/or free quarks might become abundant. The limited understanding of the matter behaviour at these high densities results in uncertainties on the equation of state.

1.3 NS basics

NSs can be isolated or be members of binary systems. In the latter the source is often powered by accretion of material lost from the companion, while in the former emission is generally sustained by rotational energy losses. The loss rate of rotational kinetic energy yields the total spin-down luminosity

$$\dot{E} = I\Omega\dot{\Omega} = -\frac{4\pi^2 I\dot{P}}{P^3}, \tag{1.3}$$

where I is the stellar moment of inertia, $\Omega = 2\pi/P$ is the angular velocity, P is the spin period, and $\dot{P}$ is the period derivative.

According to magnetic-dipole braking model [5], neutron stars rotate in vacuum at angular velocity Ω and possesses a magnetic dipole moment $\mathbf{m}$ forming an angle α with the rotation axis. The rotation is assumed to be sufficiently slow that non-spherical distortions can be ignored to lowest order. Independent of the internal field geometry, which is still unknown, outwards the magnetic field is supposed to be a dipole which is related to $\mathbf{m}$ by $\mathrm{m} = |\mathbf{m}| = B_p R^3$, where R is the NS radius and B_p is the magnetic field strength at the magnetic pole. While constant in module, the dipole direction varies in time, radiating thus energy at a rate $\dot{E} = -2|\ddot{\mathbf{m}}|^2/3c^3$ according to Larmor's formula. By introducing a coordinate system with an unit vector parallel to the rotation axis, $\mathbf{e}_\parallel$, and two mutually orthogonal unit vectors perpendicular to the rotation axis, $\mathbf{e}_\perp$ and $\mathbf{e'}_\perp$, $\mathbf{m}$ can be explicitly written as $\mathbf{m} = \mathrm{m}\ (\mathbf{e}_\parallel \cos\alpha + \mathbf{e}_\perp \sin\alpha \cos\Omega t + \mathbf{e'}_\perp \sin\alpha \sin\Omega t)$. Thus the radiate power is

$$\dot{E} = -\frac{2}{3c^3} m^2 \Omega^4 \sin^2\alpha = -\frac{2B_p^2 R^6 \Omega^4 \sin^2\alpha}{3c^3}. \tag{1.4}$$

If one assumes that the spin down of the star is caused by the magnetic field torque and that the emission process is dipole radiation, a characteristic surface magnetic field at the poles can be inferred by equating equation 1.3 with equation 1.4:

$$B_p \sin\alpha = \left(\frac{3Ic^3}{8\pi^2 R^6}\right)^{1/2} (P\dot{P})^{1/2}. \tag{1.5}$$

Considering standard values for a NS, mass $M = 1.40$ $M_\odot$, radius $R = 10$ km, and assuming $I = \frac{2}{5}MR^2 \sim 10^{45}$ g cm^2, measurements of P and $\dot{P}$ allow to determine $B_p \sin\alpha = 3.2 \times 10^{19}$ $(P\dot{P})^{1/2}$ G.

Generalizing equation 1.5 by assuming a spin-down formula $\dot{\Omega} = -K\Omega^n$, where n is called the braking index and $K = 2m^2/3Ic^3$ is a constant, the NS age can be calculated. By integrating the spin-down formula one finds

$$\tau = \frac{P}{(n-1)\dot{P}}\left[1 - \left(\frac{P_o}{P}\right)^{n-1}\right], \tag{1.6}$$

where P_o is the period at the birth. If the present period is much longer than the initial one ($P \gg P_0$) and pure magnetic dipole braking is assumed ($n = 3$), the characteristic age, a first-order estimate of the true age, is found:

$$\tau_c = \frac{P}{2\dot{P}}. \tag{1.7}$$

Different processes lead to different braking indices: a quadrupolar braking field (gravitational or magnetic) implies $n = 5$, while the ejection of an unmagnetized particle wind would result in n=1. The braking index can be directly inferred from the measurement of the star frequency and its derivatives:

$$n = \frac{\Omega\ddot{\Omega}}{\dot{\Omega}^2}. \tag{1.8}$$

The situation is more complicated for the initial period, which can be determined from equation 1.6 if the age is known and n is measured. This is only the case for the Crab Nebula for which $P_o \simeq 19$ ms.

Information on age and magnetic field are model dependent; the equations, previously introduced, are based on a simple magnetic dipole in vacuum. However, P and $\dot{P}$ are two of the primary observables; the P - $\dot{P}$ diagram (figure 1.3) encodes a great amount of information about the pulsar population and its properties, as determined and estimated from these two quantities. It is useful for following the pulsar lives. At birth pulsars appear in the upper left corner of the diagram; if the magnetic field **B** is conserved, they gradually move to the right and down, along lines of constant **B**. Pulsars with $\tau_c < 10^5$ yr are often found in or near supernova remnants, whereas older pulsars are not, either because their supernova remnants faded away or because the supernova explosions expelled the pulsars with enough speed that they have escaped from their parent supernova remnants. The pulsars occupy the largest region of the diagram with their population extending from the very short period, low $\dot{P}$ millisecond pulsars up to high $\dot{P}$, high

magnetic field pulsars that border the magnetar range. The magnetars have the highest $\dot{P}$; a more detailed classification is reported in the next section.

Although the magnetic-dipole braking model is so useful in providing physical information, the assumption that a NS rotates in vacuo is not realistic. An important point was made by Goldreich and Julian [13], who pointed out that the combination of rapid rotation plus strong magnetic fields must, by Maxwell's equations, induce electric fields, **E**, near the star surface. **E** should force charged particles to flow from the surface; consequently, a NS posses a magnetosphere. Investigating the simplest model in which the magnetic dipole moment is aligned with the rotation axis, they argued that particles in magnetosphere, threaded by magnetic field lines that close within the light cylinder, must corotate with the star. The light cylinder is an imaginary cylinder with the axis along the star rotation axis and with a radius extending out to the distance at which the corotation velocity equals the light speed; this radius is given by

$$R_{LC} = \frac{c}{\Omega} \sim 5 \times 10^9 P \text{ cm s}^{-1}. \tag{1.9}$$

In the model of Goldreich and Julian the magnetic field is largely dipolar for distance $r < R_{LC}$:

$$B \sim B_p \left(\frac{R}{r}\right)^3, \tag{1.10}$$

while at greater distance it is an outgoing-wave field associated with an electric field of magnitude $E \sim B$ and an outward Poynting energy flux $S \sim cB^2/4\pi$. The total rate of electromagnetic emission, obtained by joining the fields at $r = R_{LC}$, is

$$\dot{E} = -4\pi R_{LC}^2 S \sim -\frac{B_p^2 R^6 \Omega^4}{c^3}. \tag{1.11}$$

Therefore, whether or not the dipole field is aligned with the rotation axis, there are losses of kinetic rotational energy that supply the braking torque.

As mentioned above, the rotation of a NS possessing a magnetic field generates powerful electric fields in the space surrounding the star. According to the Goldreich and Julian's model a spinning NS has an aligned dipole external magnetic field; assuming there are no surface currents, both the normal and tangential components of **B** are continuous across the NS surface. The stellar material is supposed to be an excellent conductor, so charges must arrange themselves to cancel out the electromagnetic force within the

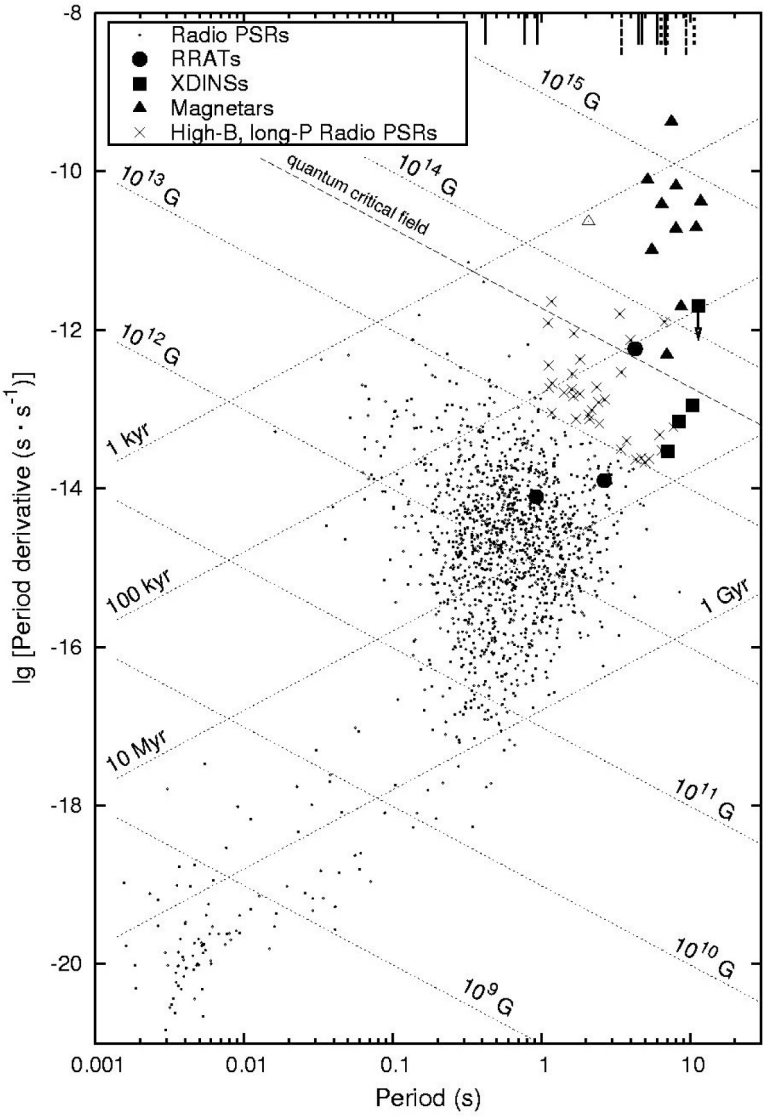

Figure 1.3: Plot of period vs period derivative. Lines of costant B and τ_c are indicated [12].

NS surface:

$$\mathbf{E} + \frac{\mathbf{\Omega} \times \mathbf{r}}{c} \times \mathbf{B} = 0, \tag{1.12}$$

this implies that $\mathbf{E} \cdot \mathbf{B}$ vanishes in the stellar interior. Inside the star the electric field is perpendicular to the magnetic field. On the other hand, outside the star $\mathbf{E} \cdot \mathbf{B} \neq 0$: the electric field develops a component which is parallel to $\mathbf{B}$ at the surface. Its magnitude is approximately $E_{\parallel} \sim R\Omega B_p/c$. Such a strong field will impart a force to both electrons and ions at the surface that exceeds the gravitational force; for instance for protons

$$\frac{\text{electric force}}{\text{gravitational force}} \sim \frac{eE_{\parallel}}{GMm/R^2} \sim 10^9, \tag{1.13}$$

where e and m are the charge and the mass of proton. Thus, particles are lifted from the surface and create a region of plasma around the star, the magnetosphere; their motion is along the magnetic field lines. Inside the light cylinder, the plasma corotates with the star; whereas magnetic field lines, that pass through the light cylinder, are open and are deflected back to form a toroidal field component. The particles, which move along these lines, are permanently lost.

1.4 The NS zoo

In the last decades mainly thanks to *Chandra* and *XMM-Newton*, two space-borne X-ray observatories, various classes of NSs have been discovered. They are a diverse population not only in their observational properties, but also in their physical ones. "They are all different species of the same animal whose magnetic field evolution and interior composition remain a mystery" [14].

NSs are classified according to the primary power source for their emission. Rotation-powered pulsars (RPPs) are powered by the loss of rotational energy due to braking by their magnetic fields; isolated neutron stars (INSs) derive their energy from the latent heat of the NS matter. Magnetars are fed by magnetic field energy, accretion-powered NSs by the energy released by matter accreting onto the NS from a binary companion. Central compact objects (CCOs) are an additional class; they are seen as soft X-ray point-like sources inside supernova remnants and have not counterparts at other wavelengths. These types occupy different areas of P-B space, as shown in figure 1.4, even though there are some overlaps. The low-mass X-ray binaries (LMXBs) overlap the millisecond pulsar (MSP) population, a subclass of RPPs; CCOs lie at the end of the RPPs, coinciding with some MSPs. The lower end of the magnetar population overlaps the upper end of the RPPs,

the INS overlaps both. The accreting X-ray pulsars have magnetic fields similar to some of the older RPPs. The magnetars have the highest surface magnetic fields, whereas the MSPs and LMXBs have very low surface fields and the shortest periods.

Rotation-powered pulsars are spinning down as a result of torques from magnetic dipole radiation and particle emission. The energy from their spin down appears as broadband pulsations from radio to gamma-ray wavelengths. Since their discovery in 1967, more than 2000 sources have been detected with periods ranging from a few ms to several seconds. There are two main families of RPPs: normal pulsars having characteristic age $\tau_c <$ 100 Myr and MSPs with $\tau_c \gtrsim 100$ Myr. Some astronomers refer to MSPs as recycled pulsars, because they are thought to be created by the recycling of an otherwise dead pulsar through the accretion of matter. There is also a growing subclass known as rotating radio transients (RRATs), discoreved recently [15]. They show a variety of transient behaviour, raging from nulling for long time periods to highly modulated pulsations.

About 10% of the total spin-down power is converted into pulsed radiation; for the majority of RPPs pulsed emission power peaks in gamma rays around a GeV, for few of them, such as Crab nebula, it is in hard X rays. Radio pulsations are easy to detect since the photon flux is high; gamma-ray pulsations can help to study the particle acceleration mechanisms in pulsar magnetosphere, because they carry away the highest percentage of the spin-down power. Many RPPs show X-ray emission, which may contain both thermal and non-thermal components. The former can be divided into pulsed and unpulsed emissions; the pulsed component comes from heated polar caps, while the unpulsed component originates from the cooling of the star, emitted from the whole surface. The non-thermal emission may arise from the magnetosphere. In same cases a pulsar wind nebula (PWN) is found to surround a RPP, it consists of high-energy particles trapped by supernova shell. It has an unpulsed emission from radio to high-energy (TeV) gamma-rays.

Magnetars are young NSs with intense magnetic fields $B \sim 10^{14}$-10^{15} G, above the so-called quantum critical field, $\mathrm{B}_{cr} = \frac{m_e^2 c^3}{e\hbar} = 4.4 \times 10^{13}$ G, at which the cyclotron energy of an electron equals the electron rest mass energy. In strong fields new processes could occur, such as one-photon pair production, vacuum polarization and photon splitting. These mechanisms influence the propagation of photon in the NS atmosphere and the spectrum of the emitted radiation. Magnetars show both steady X-ray pulsations and soft γ-ray

bursts.

Historically, magnetars are classified in two groups: anomalous X-ray pulsars (AXPs) and soft gamma-ray repeaters (SGRs). Around 1979 [16] the first SGRs were discovered and were thought to be a variant of classical γ-ray bursts. When active, they typically emit short ($\sim$0.1 s) very bright bursts recurring on different time-scales from seconds to years; rarely, they undergo dramatic instabilities producing long and giant hard X-ray and soft γ-ray flares. In the early 1980s AXPs were first discovered by *EXOSAT* as pulsating X-ray sources. They were classified as a type of accreting X-ray pulsars, but a companion and an accretion disk were not detected. The AXPs have pulsations period in a range of 5-11 s and are spinning down with large period derivatives. Their pulsed profiles are broad and very similar to those of SGRs. In the last decades, better data have become available and the separation between these two classes has become thinner, so they are no longer considered different objects. The quiescent spectra of magnetars consist of a thermal component, fit by a blackbody, at low energy ($\sim$ 0.5-1 keV) and one or more non-thermal components, fit with power laws, below 10 keV. Before they were detected, Duncan and Thompson [17] proposed a model according to which NSs can generate strong magnetic fields by dynamo action.

Central compact objects are found close to the center of supernova remnants (SNRs); their association with SNR indicates these NSs are young, $\lesssim 10^4$ yr. They show a constant X-ray emission in the few hundred eV range and this property sets them apart from AXPs and SGRs. CCOs have no binary companion and no radio/IR/optical counterparts, therefore they are not standard young radio pulsars. About 10 CCOs are presently known, only three of them have a spin period measured: PSR J0821$-$4300 in SNR Puppis A, 1E 1207.4$-$5209 in SNR PKS 1209$-$51/52, and PSR J1852+0040 in SNR Kesteven 79 [18]. The observed spectra are purely thermal, but some have multiple blackbody components. The measured radii of the emitting region, assuming blackbody spectra, are less than 1 km, much smaller than the NS radius. X-ray timing and spectral measurements suggest these sources have relatively weak surface magnetic fields in the range 10^{10}-10^{11} G; this implies that their spin period is basically the same as the natal one. Since their SNRs are young, they were probably born with low magnetic fields, which make them "anti-magnetars".

Accreting neutron stars are members of binary systems, where they can accrete from the companion, either from a stellar wind or from an accretion disk, which forms if the companion overflows its Roche Lobe. The gravitational energy from the infalling matter provides at least part of the

energy for the observed radiation and the accretion torques dominate the spin evolution.

These systems are classified according to the companion mass: in LMXBs the companion has $M_c < 1$ $M_\odot$, in the high-mass ones (HMXBs) $M_c \gtrsim 5$ $M_\odot$ and in intermediate-mass X-ray binaries (IMXBs) 1 $M_\odot \lesssim M_c \lesssim 5$ $M_\odot$. In LMXBs almost all of the radiation is emitted as X rays; some of them have steady X-ray emission, with occasional bursting behaviour while others are detectable only during their burst. These bursts are thought to be thermonuclear explosions on the NS surface, when the density of the accreted material reaches the critical point for igniting nuclear reactions. LMXBs also show quasiperiodic oscillations, the frequencies of which are the orbital frequencies of accreting matter. IMXBs and HMXBs are both bright X-ray sources and a large number show either persistent or transient X-ray pulsations. Many X-ray pulsars (about 20) [14] in these systems show absorption features in their spectra, which are thought to be produced by electron cyclotron resonant scattering.

A subclass of accreting X-ray binaries are called microquasars, made up of a compact object with a normal companion. They display properties similar to those of the quasars, such as radio jets and variability of X-ray emission. These sources undergo repeated radio, optical and X-ray flaring with associated formation of relativistic jets. Broad emission lines are also detected from their accretion disks.

Isolated neutron stars lack any observable associated supernova remnant or nebula. They appear to be thermally cooling with no emission outside the soft X-ray band, except for optical and/or UV counterparts. There are seven confirmed INSs, called 'The Magnificent Seven' and discovered by *ROSAT*, the ROentgen SATellite. For all of them weakly X-ray pulsations have been measured with periods between 3 s and 11 s. The INSs are characterized by blackbody-like emission with kT in the range $\sim$ 40-100 eV, with no power law or non-thermal components. Most INSs show absorption lines in their spectra at energies between 0.2-0.8 keV. These features have been suggested to be proton cyclotron lines or neutral hydrogen atomic transitions in a strong magnetic field. These sources offer an opportunity to study the NS surface properties thanks to their thermal spectra, which are thought to be uncontaminated by magnetospheric processes. Furthermore, X-ray spectroscopy may provide the NS radius, if the distance is known, and also its mass, if spectral features are detected at the same time. This would make it possible to put constraints on the EoS.

The Magnificent Seven are middle-aged cooling NSs. The characteristic age is a poor estimate of the true age; the former, provided by period and

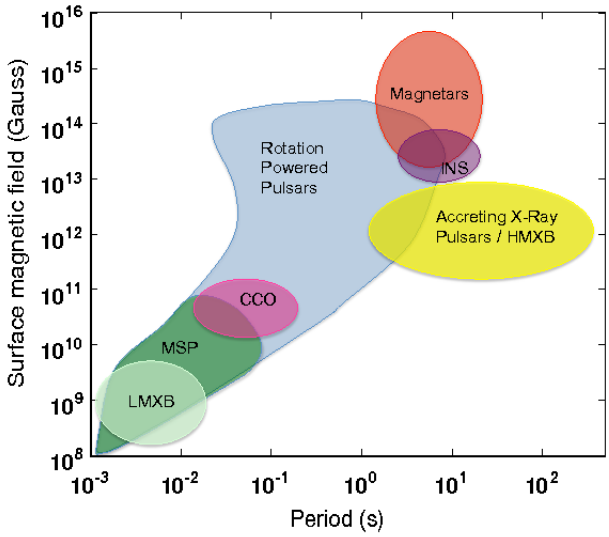

Figure 1.4: Schematic diagram of neutron star populations with respect to their periods and derived surface magnetic field strengths [14].

period derivative, is of the order of $\sim 10^6$ yr, but this estimate is longer than expected based on cooling. From standard cooling curves the observed temperature of INSs corresponds to ages of few 10^5 yr. Assuming these objects spin down by magnetic dipole radiation, magnetic field strength can be inferred obtaining values of the order of $\sim 10^{13}$ - 10^{14} G.

The X-ray luminosities of several INSs are larger than their spin-down luminosity, so rotation cannot power the observed X-ray emission. The temperatures and thermal luminosities are too high for conventional cooling at their characteristic ages. This implies an additional source of heating, such as magnetic field decay.

NSs are found in a wide variety of sources, displaying various behaviours. The aim is to unify all known classes of sources considering them as different manifestations of the same underlying physics. In the last years, interesting ideas for grand unification have been developed, for instance a theory of magneto-thermal evolution may establish the evolutionary links between different families. According to it thermal evolution and magnetic field decay are inseparable. Temperature affects crustal electrical resistivity, which in turn influences magnetic field evolution; while the decay of the field can produce heat that affects the temperature evolution. In this picture INSs

may be old magnetars, high fields of which have decayed.

Chapter 2

Magneto-thermal evolution

Observations show evidence that most nearby NSs have an anisotropic temperature distribution, which could be influenced by magnetic fields developed inside and outside of NSs. Moreover, most thermally-emitting isolated NSs have magnetic field larger than 10^{13} G; this implies that a realistic cooling model must include the effects of high magnetic fields.

The magneto-thermal evolution takes into account the coupling between temperature and magnetic field. It is essential to describe the evolution of highly magnetised NSs.

2.1 Magnetic field

Magnetic field plays an important role in NS evolution by accelerating particles, by channelling these particles or accretion flows, by producing synchrotron emission or resonant cyclotron scattering, and by providing the main mechanism for angular momentum loss from non-accreting stars. As mentioned in the previous chapter, an estimate of the surface magnetic field could be obtained from periods and period derivatives. In nearly all cases, there are no other measurements of the magnetic field strength and only indirect inferences of its geometry are possible from the pulse profile. Its magnitude is deduced to be of the order of 10^{11} - 10^{13} G in most objects, as low as 10^{8} - 10^{9} G in the old rapidly spinning millisecond pulsars, and as high as 10^{14} - 10^{15} G in the slowly spinning magnetars[1]. The association of weaker magnetic fields with older objects suggests that magnetic fields of NSs are subject to decay. However, population synthesis studies propose

[1]Magnetar magnetic field is the strongest known in the Universe. They exceed magnetic fields produced on Earth, up to 10^{7} G produced in explosions for very short time, or on other stars, up to 10^{9} G on white dwarfs.

that old pulsars have not significant magnetic field decay over their life [19], although the opposite conclusion has also been drawn [20]. To resolve this contradictory fact it is assumed that NS magnetic field is maintained by two current systems. Long living currents in the core support large-scale field and are responsible for the spin down of old pulsars; while currents in the crust support the short-lived part of the field.

Soon after birth, the gravitational collapse leaves a highly convective and rotating proto-neutron star. Its magnetic field eventually reaches a stable, ideal-MHD equilibrium with a poloidal and a toroidal component, which stabilize each other, aided by the compositional stratification of NS matter. Ideal MHD is likely a good approximation in the very early stages of NSs, in which the relevant time scales are short and the temperature is high [21]. Afterwards the temperature decreases enough for the crust to freeze to a solid state, for the neutrons of the core to become superfluid, and for the protons in at least parts of the core to become superconducting. Thus, the crust will no longer behave as a fluid. The electron currents supporting the magnetic field in the crust will carry the magnetic flux lines in a process called Hall drift, which is non-linear and non-dissipative, possibly creating currents sheets (which are places where very efficient dissipation occurs). The evolution of the magnetic field is likely to generate a Lorentz force, which perturbs the balance between pressure and gravity. This produces stresses that can break the crust if strong enough, allowing the matter and the magnetic field to rearrange. This process can explain some of the violent events in magnetars, but how it occurs has not understood yet.

The core is supposed to remain liquid; different processes can take place depending on the temperature. At high temperature, after enough times, neutrons and charged particles can convert into each other through β-decays, eventually creating a chemical equilibrium controlled by only one variable, for instance the pressure or density. As a consequence the fluid will behave as a barotropic fluid. In this state the magnetic field structure is more constrained and maybe no stable equilibria exist. If the field is too strong, it might break the crust and be largely lost from the star, otherwise the crust might help in supporting a new equilibrium structure in the core. Whereas at lower temperatures, the fluid becomes more and more degenerate, lowering the drag forces between neutrons and charged particles, so a two-model fluid becomes more applicable. The magnetic field will be coupled only to the charged particles and will force them to move relative to the neutrons in a process called ambipolar diffusion. If the charged particles are only protons and electrons, the densities of which have to satisfy the condition of charge neutrality, they will behave as a barotropic fluid and the situation is the same

of the previous case. As seen, the evolution of the magnetic field is complex and requires numerical simulations to be sorted out in more details.

The evolution of the magnetic field is summarized by the induction equation [22]

$$\frac{\partial \mathbf{B}}{\partial t} = \nabla \times \big(\mathbf{v} \times \mathbf{B}\big) - \nabla \times \left(\frac{c}{\sigma}\mathbf{j}\right) + \gamma \nabla \times \left(- \frac{\mathbf{j}}{n_e e} \times \mathbf{B}\right) \tag{2.1}$$

where $\mathbf{v}$ is a weighted average velocity of all charged particles, $\mathbf{j} = \frac{c}{4\pi}\nabla \times \mathbf{B}$ is the electric current density, n_e is the density of protons and electrons, e is the proton charge, σ is the isotropic electrical conductivity, limited by inter-particle collisions, and γ is a dimensionless factor whose magnitude and sign depends on the relative coupling of protons and electrons to neutral background.

Each term describes a mechanism that promotes the loss of magnetic flux from an isolated NS. The first represents the ambipolar diffusion; since the driving forces are proportional to B^2, this term scales as B^3 becoming more effective at high field strengths. It operates in the outer part of the core where the charged particle composition is homogeneous; the charged particle flux associated with ambipolar diffusion can be decomposed into a solenoidal and an irrotational component. The irrotational one perturbs chemical equilibrium between neutrons, protons, and electrons, thus generating pressure gradients that effectively choke it. The solenoidal component is capable of transporting magnetic flux from the outer core to the crust on a short time scale. The second term in equation 2.1 describes the Ohmic diffusion, linear in the magnetic field. It proceeds at a rate that is inversely proportional to the electric conductivity; it occurs in both the fluid core and the solid crust of a NS. This mechanism is too slow to directly affect magnetic field decay, mainly large-scale structures, because its time scale exceeds the age of the Universe. The last term describes the advection of the magnetic flux by the electric current, called Hall effect. It is non-dissipative, so it does not change the total magnetic energy and cannot by itself be responsible for magnetic field decay. It is non-linear ($\propto B^2$) and could possibly lead to small-scale structures in the solid crust, where ambipolar diffusion cannot occur. Moreover, the Hall drift can enhance the rate of the Ohmic dissipation which can become effective to limit the lifetimes of crustal currents.

External agents may also change the magnetic field of a NS:

- the strong thermal gradient in a cooling proto-neutron star can overcome the stratifying effect of the chemical gradient. At the same time,

the star has not had time to transport angular momentum and is differentially rotating. This combination acts as a dynamo, which is a mechanism proposed by Thompson and Duncan [17] to explain the existence of magnetars with very high field strengths;

- the thermal gradient can persist for a longer time in the outer crust, where it may work as a battery, giving rise to a substantial field. This may explain an increasing field in a young pulsar;
- accretion from a binary companion is a way of decreasing the magnetic dipole moment; perhaps the most interesting process is the burial of the magnetic flux by the accreted, highly conducting plasma.

2.2 NS cooling

NSs are born very hot in supernova events with internal temperature $T \sim 10^{11}$ K and gradually cool down. The cooling is realized via two channels, by neutrino emission produced in the core and by transport of heat from the internal layers to the surface resulting in the thermal emission of photons. It depends on the composition and the properties of the stellar interior, which are described by the equation of state. Given an EoS, a family of NS models can be built with different values of central density, hence different masses and radii, and the cooling of any model can be simulated. Therefore, comparing observations with models, the NS cooling theory offers an opportunity to study the NS internal structure.

The thermal evolution is described by the energy and flux equations obtained by Thorne [23]; for a spherically symmetric star, including relativistic corrections, they are

$$\frac{e^{-\lambda-2\Phi}}{4\pi r^2}\frac{\partial}{\partial r}\left(e^{2\Phi}L_r\right) = -Q + Q_h - \frac{c_T}{e^{\Phi}}\frac{\partial T}{\partial t}, \tag{2.2}$$

$$\frac{L_r}{4\pi\kappa r^2} = e^{-\lambda-\Phi}\frac{\partial}{\partial r}\left(Te^{\Phi}\right) \tag{2.3}$$

where r is the radial coordinate, Q is the neutrino emissivity, c_T is the heat capacity per unit of volume, κ is the thermal conductivity, L_r is the local radiative luminosity transported through a sphere of radius r, and Q_h represents the rate of energy production by reheating sources, associated for instance with dissipation of rotational energy. Furthermore, $\Phi(r)$ and $\lambda(r)$

are the metric functions determined from a hydrostatic NS model. The function $\Phi(r)$ specifies the gravitational red-shift, $e^{\Phi(r)} = (1 - 2Gm(r)/rc^2)^{1/2}$, while $\lambda(r)$ describes the gravitational distortion of radial scales, $e^{\lambda(r)} = (1 - 2Gm(r)/rc^2)^{-1/2}$ where $m(r)$ is the gravitational mass enclosed within a sphere of radius r. At the stellar surface, $\Phi(R) = -\lambda(R)$.

In the outermost layers (as long as electrons are nondegenerate), thermal conduction is radiative; in the crust it is provided by electrons, while in the core it is produced by electrons, neutrons, and other baryons.
The aim of the cooling theory is to calculate cooling curves, $T_s^{\infty}(t)$, which describe the evolution of surface temperature measured by a distant observer, to be compared with observations. This requires the measurement of three quantities for each NS: the effective temperature, the distance, and the age. The values of the effective temperature are obtained by fitting the observed spectra with theoretical models. Distance measurements come from a variety of techniques, such as parallax measurements and methods of radio astronomy. For sources associated with supernova remnants, the distance estimate to supernova remnants are taken as the source distance. The NS ages are inferred via their kinematic properties, their spin-down rates, or their associations with supernova remnants. With the data currently available, it is evident that there exists no single universal cooling curve followed by all NSs. NSs have a different range of masses, of magnetic field strengths and various envelope compositions, but it is not clear which of these parameters produces the dominant effect in cooling history.

In all models the thermal evolution is characterized by three stages:

1. the initial thermal relaxation stage lasts for $t \lesssim 10$ - 100 years; the crust remains thermally decoupled from the core, and the surface temperature reflects the thermal state of the crust;

2. the neutrino cooling stage lasts for $t \lesssim 10^5$ years; the crust temperature is set by the temperature of the isothermal core, which cools by neutrino emission. The neutrino luminosity L_ν is much larger than the photon luminosity L_γ. The heat, that diffuses outward from the core to the surface, gives rise to the thermal emission observed from young NSs. The main regulators of this phase are neutrino emission mechanisms[2] and the effect of baryon superfluidity on this emission;

3. beyond 10^5 years, the thermal evolution enters the photon cooling stage during which the neutrino luminosity falls below the photon luminosity.

[2]They are direct Urca and modified Urca processes which have been introduced in section 1.1.

The cooling of the core proceeds via the escape of radiation from the NS surface, hence it is sensitive to properties of the outer parts of the star.

After the thermal relaxation, the redshifted temperature $T(t) = T(r,t)e^{\Phi(r)}$ becomes constant throughout the stellar interior. Equations 2.2 and 2.3 reduce to the equation of the global thermal balance [24]:

$$C(T)\frac{dT}{dt} = -L_\nu^\infty(T) + L_h^\infty - L_\gamma^\infty(T_s) \tag{2.4}$$

where C is the total stellar heat capacity, L_ν^∞, L_h^∞, and L_γ^∞ are the total neutrino luminosity, reheating power and photon luminosity, respectively, for a distant observer.

Cooling models are divided into three categories. The standard cooling models include the effects of modified Urca and nucleon-nucleon bremsstrahlung processes of neutrino emission and predict the slowest cooling rate; the minimal cooling models take into account additional neutrino emission from the breaking and formation of Cooper pairs in the superfluid core and lead to moderate cooling rate in a limited temperature range. The enhanced cooling models result in the lowest surface temperature and the shortest thermal emission timescales. The cooling rate also depends on the composition of the envelope and of a thin layer within the envelope in which the ions are in liquid phase. As a general trend, NSs with higher central densities and with light element envelopes cool faster. From the comparison between the data and the cooling curves [25], direct Urca processes, predicted by enhanced cooling models, are inconsistent with the high temperatures observed in NSs in the 10^4-10^6 yr age range. Moreover, the high surface temperatures measured in the young NSs PSR 1E1207-52 and PSR J0822-4247 imply the presence of light elements in the envelope with no fast neutrino emission processes in the cores. Also, minimal cooling with heavy element envelopes has been excluded because of the upper limits in thermal emission from three compact objects (PSR J1124-5916, the pulsar in 3C58, and the pulsar in CTA1) and the emission observed from the Vela pulsar.
The cooling can be different for low, medium and high mass NSs. The former cool via slower processes. Numerous cooling scenarios of high-mass NSs have been proposed. The simplest assumes non-superfluid cores where direct Urca process is forbidden. It is widely thought that neutrino emission in high-mass NSs is enhanced as compared to the emission provided by the modified Urca process. An enhanced emission leads to fast cooling, allowing to explain the observations of coldest NSs for their ages. Medium-mass NSs

have an intermediate behaviour.

The cooling is influenced by many factors, among which there are the rate of neutrino emission and the heat capacity in the stellar interior. These two items depend on the composition of the NS, and the stellar structure depends in turn on the equation of state of matter at high densities. Furthermore, neutrino emission and heat capacity are also affected by superfluidity. The thermal conductivity is a crucial ingredient; it is sensitive to the presence of a light-element layer and magnetic fields in the envelope. A magnetic field makes the thermal conductivity anisotropic; the effects are twofold. Classical effects are produced by electron cyclotron motion perpendicular to the direction of the magnetic field. They do not affect the electron thermal conductivity along the field, but they can reduce it across the field. These effects are especially important near the magnetic equator, where the field is tangential to the surface and the heat is carried away from the interior across the field lines, so the equatorial regions conduct heat less well. Quantum effects are associated with the quantization of electron motion into Landau levels. If the magnetic field is strong enough, the majority of electrons occupies the lowest Landau level; this implies an enhancement of the longitudinal thermal conductivity of degenerate electrons. This effect is most pronounced near the magnetic pole, where the field is normal to the surface and heat propagates along the field lines. Quantum effects increase the local surface temperature.

2.3 Magneto-thermal evolution

As discussed above, the magnetic field affects the crustal temperature distribution. If it is too strong, it causes an anisotropy in the thermal conductivity and changes in how heat flows from the core through the crust up to the surface. Moreover, the generation of heat produced by magnetic field dissipation results in a non-spherically symmetric allocation of heating sources. It is important to solve simultaneously the induction equation and the heat transfer equation, taking into account the anisotropy of the thermal conductivity and the electrical resistivity tensor in a consistent way.

In the last years many efforts have been made to provide a self-consistent model for the coupled evolution of the magnetic field and temperature in NSs. Aguilera et al. [26] developed a 2D cooling code including the temperature evolution and the magnetic field decay, which was simulated by a phenomenological analytical formula without solving the induction equation. In Pons and Geppert [27] a spectral code follows the evolution of the magnetic

field, considering both the resistive and the Hall term, but the temperature evolution was described by an isotropic, analytical cooling law. The first 2D simulations of the fully coupled magneto-thermal evolution included only Ohmic dissipation, because of numerical difficulties in the treatment of the Hall term [28]. Viganò et al. [29] overcame these limitations and present a 2D code able to manage arbitrarily large magnetic field intensities, treating the Hall term consistently. To confront models with observational data, measurements of both age and temperature (or luminosity) of NSs are required; the number of sources which have these two quantities measured is limited. They studied a sample of forty sources, which consist of four CCOs, eight RPPs, seventeen magnetars, four high-B radio-pulsars, and the Magnificent Seven. The adopted procedure and results obtained by Viganò et al. are reported below.

The fundamental equations that govern the magneto-thermal evolution are the heat balance equation and the relativistic Hall induction equation. To take into account general relativistic effects, the standard static metric is used

$$ds^2 = -c^2 e^{2\Phi(r)} dt^2 + e^{2\lambda(r)} dr^2 + r^2 d\Omega^2,$$

where $\Phi(r)$ and $\lambda(r)$ are the metric functions introduced in the previous section. The deformations due to rotation and magnetic field are not included.

The thermal evolution is described by the following energy balance equation, which is the equation 2.2 written in a different way:

$$c_T e^{\Phi} \frac{\partial T}{\partial t} + \nabla \cdot (e^{2\Phi} \mathbf{F}) = e^{2\Phi}(-Q + Q_h), \tag{2.5}$$

where Q_h stands for the Joule heating rate per unit volume, and $\mathbf{F}$ is the heat flux which in the diffusion limit is $\mathbf{F} = -e^{-\Phi} \widehat{\kappa} \cdot \nabla(e^{\Phi} T)$. The total thermal conductivity tensor $\widehat{\kappa}$ must include the contributions of all relevant carriers, such as electrons, protons, and neutrons. The heat is transported primarily by electrons. For magnetized NSs, the electron thermal conductivity tensor becomes anisotropic: in the direction perpendicular to the magnetic field, its strength is strongly diminished, which causes a suppression of the heat flow orthogonal to the magnetic field lines. This is the reason why the thermal evolution is coupled to the magnetic field evolution. The latter is described by the relativistic Hall induction equation:

$$\frac{\partial \mathbf{B}}{\partial t} = -\nabla \times \left[\frac{c^2}{4\pi\sigma_{\parallel}} \nabla \times (e^{\Phi} \mathbf{B}) + \frac{c}{4\pi e n_e} \left[\nabla \times (e^{\Phi} \mathbf{B}) \right] \times \mathbf{B} \right], \tag{2.6}$$

where $\sigma_{\parallel}$ is the electrical conductivity in the direction of the magnetic field[3]. The magnetization parameter $\omega_B\tau_e \equiv \sigma B/cen_e$, where ω_B is the gyration frequency of electrons and τ_e is the relaxation time, affects both evolution of magnetic field and temperature. When $\omega_B\tau_e \gg 1$, $\widehat{\kappa}$ becomes very anisotropic and the Hall term dominates, transferring magnetic energy from large to small scales and allowing an interplay between poloidal and toroidal components of **B**. An important aspect is the geometry of the magnetic field: regions permeated by radial magnetic field lines are thermally connected to the interior, while zones with tangential magnetic field (equator in the dipole case) are thermally insulated.

To solve these equations a NS model is required, based on an equation of state and microphysical inputs, such as neutrino emissivity, specific heat, thermal and electrical conductivity. In general these ingredients depend on the local values of temperature, density, composition and magnetic field strength.

Results

Firstly Viganò et al. study the *cooling of weakly magnetized NSs*. They build models with heavy element envelopes (iron) and light element (hydrogen) envelopes, calculating the respective cooling curves. In general after ~ 100 yr, NSs with mass $M \lesssim 1.4$ M$_\odot$ are brighter than high-mass NSs ($M \gtrsim 1.4$ M$_\odot$). In the latter the direct Urca processes start and result in fast cooling before one hundred years. Within the low-mass family, cooling curves are similar at early ages; the differences at $t \sim 10^2$ - 10^3 yr are due to the transition of neutrons in the core to a superfluid state. All these events depend on the EoS employed. Light-element envelope models predict luminosities around 10^{33} - 10^{34} erg s^{-1} for a long period, up to several 10^4 yr; while for models with heavy-element envelopes, the luminosity drops below 10^{33} erg s^{-1} a few thousand years after birth. Furthermore, in the photon cooling era NSs with light-element envelopes are much cooler than those with iron envelopes.

For all weakly magnetized models, after ~ 1 Myr, the surface temperature goes below 20-30 eV, the luminosity has dropped below 10^{31} erg s^{-1}, and the star becomes invisible to X-ray observations.

Cooling of strongly magnetized NSs is affected by numerous factors, for

[3]In presence of strong magnetic fields, σ becomes a tensor and Ohm's law must be written as $\mathbf{j} = \widehat{\sigma}\mathbf{E}$ or equivalently $\mathbf{E} = \widehat{R}\mathbf{j}$, where $\widehat{R} = \widehat{\sigma}^{-1}$ is the resistivity tensor. This tensor can be decomposed in symmetric and antisymmetric parts. The former is isotropic and determined by $1/\sigma_{\parallel}$; the antisymmetric part can be represented by a vector proportional to **B**.

instance the initial magnetic field and its geometry. A newly born NS has an unknown initial configuration of the magnetic field. Three models with different geometries are built: type A has a crustal confined magnetic field, type B is characterized by a core-extended magnetic field, and type C is a hybrid case where a double system of currents supports a large-scale, core-extended dipole and an additional, stronger crustal magnetic field. Each family is parametrised by the intensity of the dipolar component at the pole and the maximum intensity of the toroidal magnetic field at any point. What governs the evolution of the magnetic field is where the bulk of currents circulates, because their location determines the dissipation rate.

These models follow different evolutions. We consider a model of type A, with only dipolar component; the first effect of the Hall term is to couple the toroidal and poloidal magnetic field components, so if the former is zero at the beginning, it is soon created. Therefore, after $\sim 10^3$ yr, the poloidal dipolar field has developed a quadrupolar toroidal magnetic field. Another effect of the Hall term is that currents are gradually drained towards the inner crust, where they can last more. The presence of tangential components of B insulates the surface from the interior. For a dipolar geometry, the magnetic field is nearly radial at the pole, which are thermally connected with the interior, whereas the equatorial region is insulated by tangential magnetic field lines. If the crust is colder than the core, the polar regions will be hotter than the the equatorial regions; if Ohmic dissipation heats up the equatorial regions, they remain hotter than the poles. Analysing a model of type A with also a toroidal component, there are significant differences from the previous case. In particular, the symmetry with respect to the equator is broken because the vertical drift of the toroidal component acts towards the north pole.

In the core-extended configuration with no toroidal component, the field in the core is almost frozen due to the high electrical conductivity of the interior. Some weak Hall activity is developed at the bottom of the crust, but the maximum value of the toroidal field generated is about one order of magnitude weaker than the one developed in model of type A. Moreover, the reduced heat deposition in the crust results in a cooler surface compared to all the other models, similar to the low field cooling models. The intermediate case shows an evolution similar to the one of the model A with Hall dynamic fed by crustal currents. The relevant difference is that at late times there will be a long-lasting magnetic field in the core.

The dependence on the NS mass and microphysical parameters of magnetic field can be explored. Comparing the evolution of the dipolar component of the magnetic field for different NS masses and the same Q_{imp} in the pasta region (Q_{imp} is the parameter which describes the electron-impurity

collisions), there are no significant differences. The small quantitative differences are due to the thickness of the crust, which varies with the NS mass. In the inner crust, electron-impurity scattering influences the resistivity at low temperature, so Q_{imp} controls the evolution at the late time when the star is cold. If a low value of Q_{imp} in the pasta region is set, the dissipation at late times is much slower. Another consequence of a low impurity parameter is that, since the star age is much shorter than the magnetic field dissipation timescale, a similar asymptotic value of the magnetic field is reached for all NSs born as magnetars.

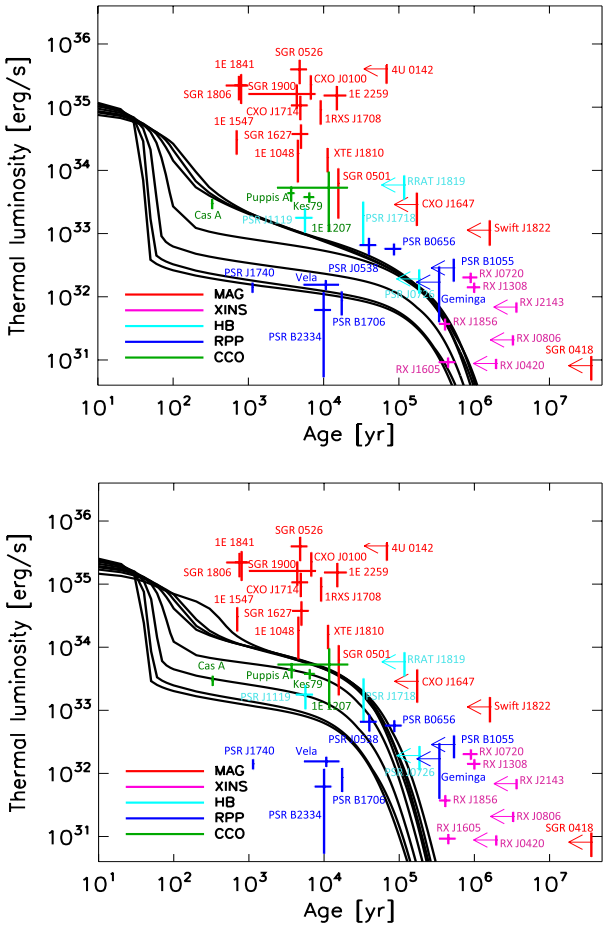

Figure 2.1: Luminosity versus age for B=0 NS models. The graphics show cooling curves for 8 masses (lines form top to bottom 1.10, 1.25, 1.32, 1.40, 1.48, 1.60, 1.70, and 1.76 $M_\odot$) compared with data. *Top*: models with iron envelopes. *Bottom*: models with light-element envelopes [29].

Unification of the NS zoo

The main aim is to find theoretical models which can describe the observational data. The sample consists of isolated NSs with detected surface thermal emission. All the sources are classified in three groups according to the initial magnetic field strength.

NSs with initial magnetic field B $\lesssim$ 10^{14} G: this group includes all RPPs, all CCOs, two high-B radio-pulsars and two of the Magnificent Seven. The cooling curves for weakly magnetised NSs are consistent with all data within the uncertainties in the inferred ages and luminosities.

In the aftermath of small spin-down rate, CCOs have present period similar to the initial one. The weak inferred magnetic field contrasts with the observed surface anisotropies and high luminosities of the sources in the SNR Kes 79 and Puppis A. Light-element envelope models can explain their age and luminosity, but not the large anisotropy. It is proposed the hidden magnetic field scenario[4] to describe the anisotropy of these sources. A few sources, such as Vela pulsar and PSR B2334, show evidence of enhanced cooling, which can happen only for high mass ($M \gtrsim 1.5$ M$_\odot$) with the EoS employed.

NSs with initial magnetic field B $\sim$ 1 - 5 $\times$ 10^{14} G: this group consists of two high-B pulsars, eleven magnetars and five of the Magnificent Seven.

Few sources could be compatible with non-magnetized cooling curves, whereas many others are too luminous and require an additional heating source. For the two most luminous objects, 4U 0142 and 1E 2259, it is difficult to reconcile the observed timing properties and luminosity, even with more extreme models. Their luminosity can be explained by very high magnetic field, while the time properties are more consistent with initial $B \sim 3 \times 10^{14}$ G.

NSs with initial magnetic field B $\gtrsim$ 10 ^{14} G: this group includes eight magnetars.

These objects are characterized by the highest luminosity, barely compatible with the cooling curves with iron envelope for initial magnetic field of the order of $\sim 10^{15}$ G. However, for the same value of B a light-element envelope is able to account for the luminosity of even the brightest sources. From the $P - \dot{P}$ diagram these extreme objects do not appear to have older

[4]The object has a subsurface magnetic field, which has been screened by the initial fallback of the supernova debris onto the NS.

descendants; they show hard X-ray, non-thermal emission and unreliable estimate of the dipolar magnetic field from timing properties. It is suggested that, for same of them, the magnetosphere could play an important role in affecting luminosity and timing properties.

NSs have displayed different observational properties, but only in the last years, thanks to increasing data, a wish of a grand unification has been developed. Including for the first time the Hall term, Viganò's work is a starting-point for this unified picture, according to which the variety in NS zoo can be understood thanks to a few intrinsic differences, such as mass, age, and initial magnetic field. In next years deeper observations and discoveries of magnetars are required in order to improve comparisons with data and reduce the uncertainties of the theoretical models.

Chapter 3

The Magnificent Seven and absorption features

In this chapter the properties of the seven thermally-emitting, nearby, isolated neutron stars are described. They are also known as The Magnificent Seven (M7 hereafter). These sources are characterized by a blackbody spectrum, but most of them show broad absorption features, which represent the key points of my work. I investigate the nature of them, focusing on the possibility that they are due to inhomogeneous surface temperature distributions.

3.1 The Magnificent Seven

The M7 were discovered by *ROSAT*, a X-ray observatory launched on June 1^{st}, 1990 and deorbited on 2011. As likely products of supernova events which occurred in the nearby OB associations of the Gould Belt, these sources are located within a few hundred parsecs of the Sun: typical distances are less than $\sim$ 500 pc [30]. They are isolated, in fact they show neither association with supernova remnant nor evidence for a binary companion. The M7, known also as XDINSs (X-ray dim isolated neutron stars), are different from the other isolated NSs, because their X-ray spectra show only thermal emission with typical temperatures in the range $\sim$ 50-100 eV, without hard power-law component often observed in other isolated NS sources. The X-ray emission is believed to come directly from the NS surface and is not influenced by accretion or magnetospheric activity. The brightest source RX J1856.5-3754 is compatible with a perfect blackbody with hints for a second cold component [31]. Its spectrum is puzzling since radiative transport trough a NS atmosphere causes noticeable deviations from a blackbody. Therefore,

it is suggested that this Planckian spectrum may arise in a bare NS, that is a NS without an atmosphere [32]. An alternative possibility is to assume a condensed matter surface, liquid or solid, which might produce a nearly blackbody distribution. Such a situation may occur at sufficiently low temperatures and/or high magnetic fields; with a temperature of $kT \sim 61$ eV, RX J1856.5-3754 is the coldest one of the XDINSs and has a magnetic field of the order of 10^{13} G.

A prime reason for studying the M7 is the hope of constraining fundamental physics at very high densities; the overall goal is to determine the equation of state of ultra-dense matter and to this end it is necessary to measure simultaneously the NS mass and radius. If a star emits a blackbody radiation from its surface of radius R at homogeneous temperature T, the observed flux at distance D is $F = \sigma T^4 (R/D)^2$, where σ is the Stefan-Boltzmann constant. If distance is known and temperature can be deduced from spectral analysis, the previous relation yields the star radius. With their Planckian spectra, the M7 are the ideal targets for this purpose.

Timing studies have shown that the M7 rotate slower ($P \sim$ 3-12 s) and have higher magnetic field ($B_{dip} \sim 10^{13}$ G, as inferred assuming that the source spins down by magnetic dipole radiation) than the bulk of radio pulsars. This places them at the end of the radio pulsar distribution in the P - $\dot{P}$ diagram (fig. 1.3). However, the $\dot{P}$ measurements still indicate field strengths below those of the magnetars. The discovery of a few radio pulsars with similar magnetic field strengths and long periods [33] shows that radio emission can still occur at field strengths close to the quantum critical field. Therefore, it remains unclear if the M7 exhibit no radio emission at all or if we do not detect it because their radio beam is very narrow due to their large light cylinder radius and does not cross the Earth [12].

From P and $\dot{P}$ measurements, the characteristic age can be inferrred; for all the M7 an estimate of τ_c is available (table 3.1). For instance, τ_c is 1.9 Myr and 1.5 Myr for RX J0720.4-3125 and RX J1308.6+2127, respectively. They are substantially longer than expected based on cooling: the observed temperatures around 90 eV correspond to ages of a few 10^5 yr. Even if one takes into account that the blackbody temperature overestimates the effective temperature, this problem remains. At 1.5 Myr the effective temperature should be below 20 eV. For RX J0720.4-3125 there is an additional age estimate from kinematics; from its proper motions it is 7×10^5 yr. The discrepancy between the two ages may mean that τ_c is a poor estimate of the true age of the star. Also for RX J1856.5-3754, the kinematic age of 4.2×10^5 yr, derived from proper motion, is lower than the characteristic

age, $\tau_c = 3.8$ Myr, but it is in agreement with the cooling age, as computed within standard cooling scenario. A recent study discovers pulsations from RX J1605.3+3249, allowing to derive its characteristic age, $\tau_c \sim 3.4 \times 10^4$ yr. It is deviant from the typical few Myr measured for the other sources and implies a short evolutionary time scale that is inconsistent with the kinematic age, 4.5×10^5 yr, derived from proper motion studies.

The lightcurve shapes are quasi-sinusoidal and single-peaked. However, RX J0420.0-5022 shows evidence for a skewness in the pulse profile with a slower rise and a faster decline and RX J1308.6+2127 displays a double-peaked lightcurve.

The M7 were considered to be steady source; RX J0720.4-3125 is the only one which has shown long-term variations of its spectral and temporal properties on time scales of years. From observations in the period 2001-2003, the total flux stayed more or less constant, whereas the temperature increased and the pulse profile changed; in the following years the temperature has decreased. This behaviour could be explained either by free precession, which predicts cyclic pattern, or a glitch that occured at MJD = 52866 ± 73 days. Recent data do not support a cyclic behaviour with a period in the 7 to 14 year range in the spectral and timing properties of the source. Instead timing variations suggest a single sudden event and the spectral parameters changed significantly around the proposed glitch time [34].

If M7 are supposed to emit a single blackbody spectrum at all wavelengths, the expected luminosity in the optical band is

$$L_{opt} \sim L_X \times 10^{-5.5-\log(kT/100\ \mathrm{eV})},$$

where L_X and T are the X-ray luminosity and temperature. As a consequence, their optical counterparts are very weak, with magnitudes $\gtrsim 25$. The first among the M7 detected in the optical has been the brightest one: RX J1856.5-3754. Now, thanks to *Very Large Telescope* and *Hubble Space Telescope* observations, all seven sources have confirmed optical counterparts [35]. As expected by a thermally emitting surface, the optical data follow a λ^{-4} law. However, the optical fluxes are a factor ~ 5 - 10 in excess of the extrapolation at low energies of the X-ray blackbody best fit: this property is known as optical excess. In [35] it was found that most objects have optical excesses between 5 and 12, but that one object, RX J2143.0+0654, exceeds the X-ray extrapolation by a factor of more than 50 at 5000 Å, and that this is a robust estimate (i.e. it accounts for uncertainties in the X-ray data). In order to explain the optical excess, some suggestions were put forward. It can be understandable in the resonant cyclotron scattering model, as shown

in [36]. If we consider the M7 as bare NSs, there is another possible explanation [37]: a bare NS can be covered by a thin gaseous layer, which may have been acquired by the star accreting a small quantity of the interstellar hydrogen. Free-free absorption dominates over scattering, because the albedo is very small at optical wavelengths. The free-free absorption depth at optical wavelengths is a factor ~ 200 larger than in the X-rays: the gaseous layer is expected to be optically thin in the X-rays and thick to optical photons. This implies that the bare surface X-ray spectrum traverses the layer with no modifications, whereas at optical energies the spectrum is close to the Rayleigh-Jeans tail of a blackbody at the layer temperature.

Thanks to the detection of the optical counterparts, it was possible to measure the proper motions and, only for two sources, the parallax. The proper motion of RX J1856.5-3754, RX J0720.4-3125 and RX J1605.3+3249 are in the range $\sim$ 100 - 300 mas yr^{-1}. Distances from parallax measurements are 161^{+18}_{-14} pc for RX J1856.5-3754 and 330^{+170}_{-80} pc for RX J0720.4-3125. These values are compatible with the distances of 135±25 pc and 255±25 pc inferred from the models of 3D distribution of the hydrogen column density developed by Posselt et al. [38].

Source	kT_∞ (eV)	P (s)	$\log(\frac{dP}{dt})$ ($s^{-1}s$)	$\log(\tau_c)$ (yr)	$\log(B_{dip})$ (10^{13} G)	Reference
RX J1856.5-3754	61	7.06	-13.527	6.58	13.17	[1]
RX J0720.4-3125	84-94	8.39	-13.156	6.28	13.39	[2]
RX J1605.3+3249	100	3.39	-11.796	4.53	13.87	[3]
RX J1308.6+2127	93	10.31	-12.951	6.16	13.54	[4]
RX J2143.0+0654	104	9.43	-13.398	6.57	13.29	[5]
RX J0806.4-4123	95	11.37	-13.260	6.51	13.40	[6]
RX J0420.0-5022	48	3.45	-13.553	6.29	13.00	[7]

Table 3.1: Overall properties of M7. The sources are sorted by decreasing flux. T_∞ is the temperature measured by a distant observer, B_{dip} is the magnetic field inferred by assuming that the source spins down by magnetic dipole radiation. References: [1] van Kerkwijk and Kaplan (2008); Mignani et al. (2013); [2] Hohle et al. (2012); [3] Pires et al. (2014); [4] Harbel et al. (2003); Schwope et al. (2007); [5] Zane et al. (2005); Kaplan and van Kerkwijk (2009); [6] Kaplan van Kerkwijk (2009); [7] Kaplan and van Kerkwijk (2011).

The M7 may also have some links with other classes of pulsar-like objects, such as magnetars and rotating radio transients (RRATs). With the latter they share values of periods, period derivatives, estimated ages, spatial

distribution, and lack of persistent pulsed radio pulsar emission. To observe X-ray emission from RRATs is difficult because they are more distant (about a factor 10) than M7, and bursting RRAT-like emission from the M7 have not be detected [39]. However, this non-detection does not necessarily mean that there is no relationship between these two classes. The M7 are likely to be quite strongly magnetized neutron stars; perhaps they could be old magnetars, providing an evolutionary link between the different NS classes.

3.2 Absorption features

Although a thermal spectrum in the X-ray band provides a good description for the spectral energy distribution of the M7, features in absorption have been found in most of the sources thanks to *XMM-Newton* observations. These deviations from a perfect Planckian spectrum are detected in five XDINSs; the exceptions are the softest members, RX J1856.5-3754 and RX J0420.0-5022, even if an absorption line at energy ~ 0.3 keV in the spectrum of the latter has been claimed [40]. The properties of the features are quite similar in the different sources: they are centred at energies of some hundreds eV and are broad. They are modelled by a Gaussian, centred at energy E_0 with width σ. As shown in table 3.2, RX J1308.6+2127 exhibits the deepest spectral line, while RX J0806.4-4123 and RX J1605.3+3249 show weak spectral features at $\sim$ 300-400 eV. The width σ is generally $\sim$ 70-170 eV and the equivalent width E_w ranges between $\sim$ 30 eV and 150 eV. Absorption features change with spin phase, as in RX J1308.6+2127 and in RX J0720.4-3125. In the latter, the equivalent width follows the long-term evolution of the source and correlates with the blackbody temperature.

M7 are not the only isolated neutron stars which show absorption features in their spectra. In the spectrum of the bright CCO 1E 1207.4-5209 two features were detected, centred near 0.7 keV and 1.4 keV [41]. The rotation-powered radio pulsar PSR J1740+1000 [42] and the highly magnetized rotating radio-transient PSR J1819-1458 [43] have absorption lines at slightly higher energies than M7, E_0 is $\sim$ 550-650 eV and $\sim$ 1120 eV, respectively. Among the magnetars, there are only a case: SGR 0418+5729 shows a feature with $E_0 \sim 2$ keV [44]; variations in the line as a function of the rotational phase as large as in this source have not been seen in no other.

The detection or absence of these spectral lines may constraint the chemical composition and/or magnetic field of the star.

The origin of absorption features is unclear; they can be understood in the

Source	N_H (10^{20} cm^{-2})	E_0 (eV)	$\lvert E_w \rvert$ (eV)	$\log(B_{cyc})$ (10^{13} G)
RX J0720.4-3125	1.0	311	0-70	13.75
RX J1605.3+3249	0	400	70	13.92
RX J1308.6+2127	3.7	390	150	13.60
RX J2143.0+0654	2.3	750	50	14.15
RX J0806.4-4123	0.9	486	30	13.96

Table 3.2: Broad spectral features in the X-ray spectra of XDINSs, as found in literature.

context of proton/electron cyclotron resonances and/or atomic transitions in a magnetised atmosphere.

According to the first hypothesis, assuming that spectral features are proton cyclotron lines, an estimate of the magnetic field can be derived from the following formula

$$E_0 = 0.63(1+z)^{-1}\frac{B_{cyc}}{10^{14}\mathrm{G}},$$

where $(1+z)^{-1} \sim 0.8$ is the gravitational red-shift factor at the star surface. The values of B inferred assuming magneto-dipolar braking (table 3.1) are in rough agreement with those obtained from the line energy (table 3.2).

As discussed in [45], the feature energies can be easily matched by invoking hydrogen or helium atmosphere; gaseous atmospheres composed of heavier elements appear to be excluded by the lack of large number of features. The presence of a hydrogen atmosphere has often been considered by default, since if any hydrogen is present, gravitational settling will ensure it floats to the surface. In strong magnetic field the binding energies of atoms increase; for temperatures and fields appropriate for XDINSs, a fraction of up to 10% of neutral H will be present. According to some model-atmosphere calculations, at 10^6 K and 10^{13} G the lines from neutral hydrogen have larger equivalent width than the proton cyclotron lines; at lower temperatures or stronger magnetic fields, the fraction of neutral H increases and the difference becomes larger.

As shown in figure 3.1, the features that might be produced in H atmosphere are the electron and proton cyclotron lines, the bound-bound and bound-free transitions of neutral hydrogen relative to the ground state. In the figure the two vertical lines indicate the magnetic field strength inferred from timing for RX J0720.4-3125 and RX J1308.6+2127. From those, it follows that if these two sources have H atmosphere, the features are most

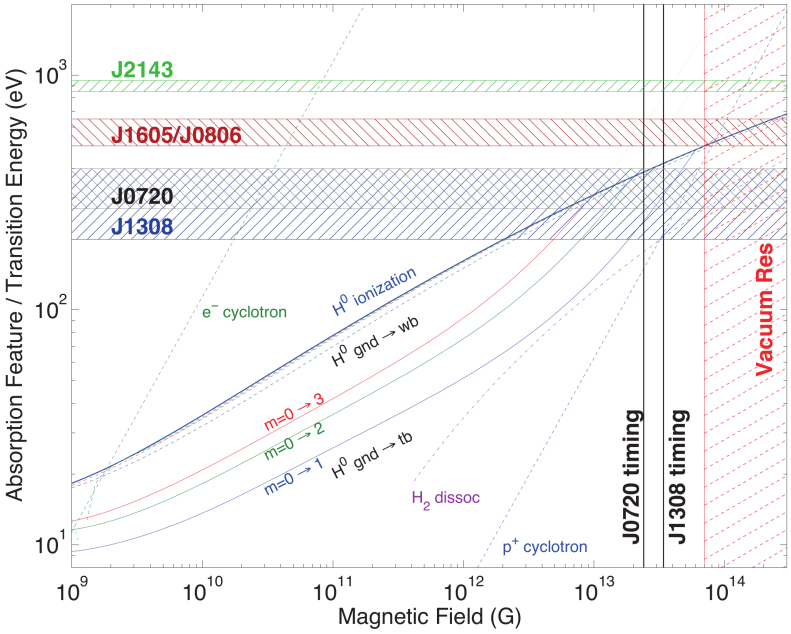

Figure 3.1: Energy versus magnetic field for electron and proton cyclotron, ground state to tightly bound (tb) or weakly bound (wb) states. The hatched bands show the energy of the main absorption features for the XDINSs. The two vertical lines indicate the dipole field strengths obtanained by timing. The sources are labeled with short-hand notation [45].

likely due to the transition from the ground state to the first excited tightly bound state of neutral H, perhaps in combination with the proton cyclotron line. The features in RX J1605.3+3249 and RX J0806.4-4123 could result from the same transitions or from the ionisation edge; in either case the implied magnetic field strength is close to 10^{14} G. For RX J1605.3+324 the line is weaker than that of RX J0806.4-4123. Van Kerkwijk et al. [46] suggest this might be due to the effect of vacuum resonance mode conversion, which tends to weaken features for fields in excess of $\sim 7 \times 10^{13}$ G. Finally, for RX J2143.0+0654, the line energy of ~ 0.7 keV is higher than what is observed in the other sources and of any transitions in neutral H. It is thus not clear whether the line could be due to neutral H; instead, it can be a proton cyclotron line in a field of just over 10^{14} G. For these field strengths, the features should be strongly weakened by vacuum resonance mode conversion, but not necessarily disappear.

If all of the hydrogen is burnt in the first years ($\sim 10^5$ yr) of a NS life, an atmosphere composed by helium might be left. For a few 10^{13} G, the

transition energies are in the range of features are observed in the XDINSs.

Three sources show some evidence for harmonically spaced lines. Apart from the line at 0.4 keV, RX J1605.3+324 exhibits other two features at 0.78 keV and 0.59 keV, energies that are in a 2:3:4 ratio with that of the stronger line. This phenomenon is also found in RX J1308.6+2127 and RX J0806.4-4123. It would appear tempting to interpret these features as proton cyclotron lines, because they are naturally harmonically spaced. However, it is difficult to see how this could be possible, since the higher harmonics are expected to be weak: the oscillator strength for the harmonic would be a factor $E_{line}/c^2 m_p$ weaker than that for the fundamental, where m_p is the proton mass.

The idea that XDINSs have pure hydrogen atmosphere appears difficult to reconcile with the spectrum of RX J1856.5-3754, which is featureless and well represented by blackbody emission.

Another explanation for absorption features has been proposed by D. Viganò et al. [1]. They evaluate the hypothesis that spectral distortions from a pure blackbody spectrum can be induced by inhomogeneous temperature distributions of the neutron star surface. These temperature inhomogeneities can be inferred from measurements of small emitting blackbody areas in a number of isolated NSs and are theoretically predicted, for instance, by anisotropic thermal conductivity induced by the presence of strong magnetic fields and by magnetospheric particle bombardment. Because of many theoretical uncertainties, such as the magnetic field geometry, it is not possible to make specific predictions for what the temperature distribution on the NS surfaces should be, and each case needs to be studied on its own.

They consider several axisymmetric surface temperature distributions and numerically compute their general relativistic spectra. In order to build surface temperature profiles, they have used the most updated envelope models with prescribed values of crustal temperature and magnetic field. From computed spectra, synthetic observed spectra have been simulated and analysed in the standard way. In some simulated spectra an absorption feature appears and it has E_0 and E_w values similar to the observed ones. These models have been directly tested for a particular source, RX J0806.4-4123. Its observed spectrum is fitted with a blackbody component plus a Gaussian; hereafter a model of such type is referred to as BB+line model. The best-fit BB+line model gives χ^2_ν=1.36, where χ^2_ν is χ^2 normalized by the number of degrees of freedom. Several different temperature distributions, with one or two hot spots, are able to fit the spectrum better than the previous model; indeed one of them fits the spectrum with χ^2_ν=1.18, improving the goodness of the fit.

The contribution to spectral features from inhomogeneous temperature distributions can be significant and this should be accounted for in combination with more sophisticated emission models.

3.3 Phase-averaged flux

The aim of this work is to test the model of Viganò et al. in the case of other M7 which show a feature in absorption. I apply the method, described above, to the sources RX J0720.4-3125, RX J1605.3+3249, RX J1308.6+2127, and RX J2143.0+0654.

First of all it is necessary to calculate the observed photon flux and to choose a surface temperature profile. The flux is computed using the formalism developed by Turolla and Nobili [47], who study the pulse profiles from thermally emitting spots on the NS surface.

In this work I employ a NS with mass $M = 1.4$ $M_\odot$ and radius $R = 15$ km, yielding a gravitational red-shift $(1 - R_s/R)^{1/2} = 0.851$, where $R_s = 2GM/c^2$ is the Schwarzschild radius. An observer at distance $D \gg R$ measures a radius $R_\infty = R/(1 - R_s/R)^{1/2} = 17.6$ km. A spherical coordinate system $(r,\, \theta,\, \phi)$ is introduced with the origin at the center of the star; the line of sight (LOS; unit vector $\widehat{\mathbf{l}}$) coincides with the polar axis.

Because of general relativistic effects, photon trajectories are not straight lines, in fact the rays, which reach the observer, leave the surface with respect to the local normal at an angle $\alpha \neq \theta$ (figure 3.2.a). Beloborodov's approximation [48] provides a simple link between these two angles without resorting to numerical techniques,

$$1 - \cos\alpha = (1 - \cos\theta)\left(1 - \frac{R_s}{R}\right). \tag{3.1}$$

Thanks to this formula, the total flux emitted by a spot of area S is given by the integral

$$F_\nu = \left(1 - \frac{R_s}{R}\right)^2 \int_{S_V} I_\nu \left[\frac{R_s}{R} + \left(1 - \frac{R_s}{R}\right)\cos\theta\right] \frac{dS}{D^2}, \tag{3.2}$$

where S_V is the visible part of the emitting region, I_ν is the specific intensity, and $dS = R^2 \sin\theta d\theta d\phi$. The observed flux is the sum of two contributions: the first proportional to the surface area and the second to the projected area of the visible part of the emitting region. The former is a relativistic

correction, while the latter corresponds to the Newtonian expression, besides the factor $(1 - R_s/R)$. Therefore, once the geometry is fixed, calculating the flux is reduced to determine S_V and to compute the two following integrals

$$I_p = \int_{S_V} I_\nu \cos\theta \sin\theta d\theta d\phi, \qquad I_s = \int_{S_V} I_\nu \sin\theta d\theta d\phi. \tag{3.3}$$

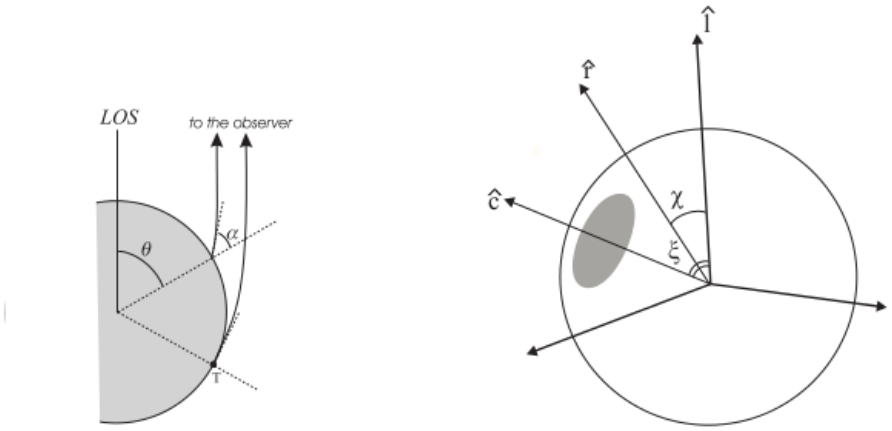

(a) **(b)**

Figure 3.2: (a): schematic view of ray propagation [47]. (b): general configuration of χ and ξ with a single cap.

The specific intensity I_ν describes the distribution of the locally emitted photons. I assume it is a blackbody distributions, thus $I_\nu \propto E^2 \times (\exp(E/k_B T) - 1)^{-1}$ where k_B is the Boltzmann constant and T is the temperature of the emitting area. If the region emits at a constant temperature, I_ν becomes the Planck's function $B_\nu(T)$ which does not depend on the angles θ and ϕ. As a consequence the two integrals can be evaluated in terms of elementary functions; for more details see [47]. Whereas if there is a meridional gradient of temperature, $T = T(\theta)$, the specific intensity I_ν depends on angles and the integrals have to be solved numerically. In my analysis both cases are treated and I create temperature profiles *ad hoc* for each source.

Regarding the geometry, I consider a NS with one or two hot spots. The spot is a circular cap of semi-aperture θ_c and center at θ_0 ; in the case of two caps, they are antipodal and have the same semi-aperture and temperature distribution.

In 3.3 the ϕ-integral is immediate:

$$I_p = 2\int_{\theta_{min}}^{\theta_{max}} I_\nu \cos\theta \sin\theta \phi_b(\theta) d\theta, \qquad I_s = 2\int_{\theta_{min}}^{\theta_{max}} I_\nu \sin\theta \phi_b(\theta) d\theta, \quad (3.4)$$

where $\phi_b(\theta)$ is the cap boundary and θ_{max}, θ_{min} are the colatitude limits of integration. Thanks to geometrical considerations it follows that

$$\cos\phi_b = \frac{\cos\theta_c - cos\theta_0 \cos\theta}{\sin\theta_0 \sin\theta}. \quad (3.5)$$

This formula defines ϕ_b in the range $|\theta_0 - \theta_c| < \theta < \min[\theta_0 + \theta_c, 2\pi - (\theta_0 + \theta_c)]$. If the LOS intersects the emitting region, the previous θ-range is not sufficient to cover the entire spot. The possible intersections are at $\theta = 0$ or π; in order to account the missing part it needs to sum up the range $0 \leqslant \theta \leqslant |\theta_0 - \theta_c|$ of $2\pi - (\theta_0 + \theta_c) \leqslant \theta \leqslant \pi$, respectively.

From equation 3.1, for each point of the star surface it has to be $\cos\alpha \geqslant 0$ and the terminator lies at $\alpha = \pi/2$. Terminator colatitude is given by $\cos\theta_F = (1 - R/R_s)^{-1}$. To consider all cases, which include the intersection or not between the cap and the terminator, the colatitude limits are $\theta_{max} = \min(\theta_0 + \theta_c, \theta_F)$ and $\theta_{min} = \min[\max(0, \theta_0 - \theta_c), \theta_F]$.

For my purpose, it is necessary to compute the phase-averaged number flux. A NS rotates with angular velocity $\Omega = 2\pi/P$, where P is the spin period; let $\widehat{\mathbf{r}}$ be a unit vector parallel to the rotation axis. Angles χ and ξ are introduced; they are the angles that the rotation axis makes respectively with the LOS and the cap axis (unit vector $\widehat{\mathbf{c}}$), i.e. $\cos\chi = \widehat{\mathbf{r}} \cdot \widehat{\mathbf{l}}$ and $\cos\xi = \widehat{\mathbf{r}} \cdot \widehat{\mathbf{c}}$ (figure 3.2.b). Since the cap corotates with the star, the vector $\widehat{\mathbf{c}}$ rotates around $\widehat{\mathbf{r}}$, keeping ξ constant; as a consequence θ_0 changes in time. θ_0 can be expressed in terms of χ, ξ, and $\gamma = \Omega t + \gamma_0$, which is the phase angle swept by the star during its rotation (γ_0 is an arbitrary initial phase),

$$\cos\theta_0 = \cos\chi\cos\xi - \sin\chi\sin\xi\cos\gamma. \quad (3.6)$$

From equation 3.2 the phase-averaged flux can be computed as an integral over the rotational phase γ. I focus my analysis on flux calculated with $\chi = 30^\circ$ and $\xi = 70^\circ$; since formula 3.6 is invariant by exchanging χ and ξ, the case with $\chi = 70^\circ$ and $\xi = 30^\circ$ is symmetric respect with the previous one.

In order to calculate the total observed phase-averaged flux emitted by a spot a program in IDL (Interactive Data Language) is written. The parameters I change in the program are the semi-aperture θ_c and the temperature

profile of each cap. If I consider a NS with a thermal map made of one spot at temperature T_1 while the rest at temperature T_2, the total flux is obtained subtracting from the larger cap the contribution of the inner spot at the temperature T_2 and adding the latter at at the respective temperature. The same reasoning is applied if the NS has two spots at T_1. The program gives as output a text file. It consists of three columns that include the energy values, which define the bin, and the total phase-averaged flux for each bin. This file is imported in *Xspec* and used as a model with which I fit the observations.

Moreover, the program can also compute the pulse profile in a given energy band. It is obtained integrating equation 3.2 over frequencies. Figure 3.3 shows the pulse profile emitted by two antipodal spots of semi-aperture 3° and 12° at constant temperature 0.2 keV for $\chi = 70°$ and $\xi = 30°$.

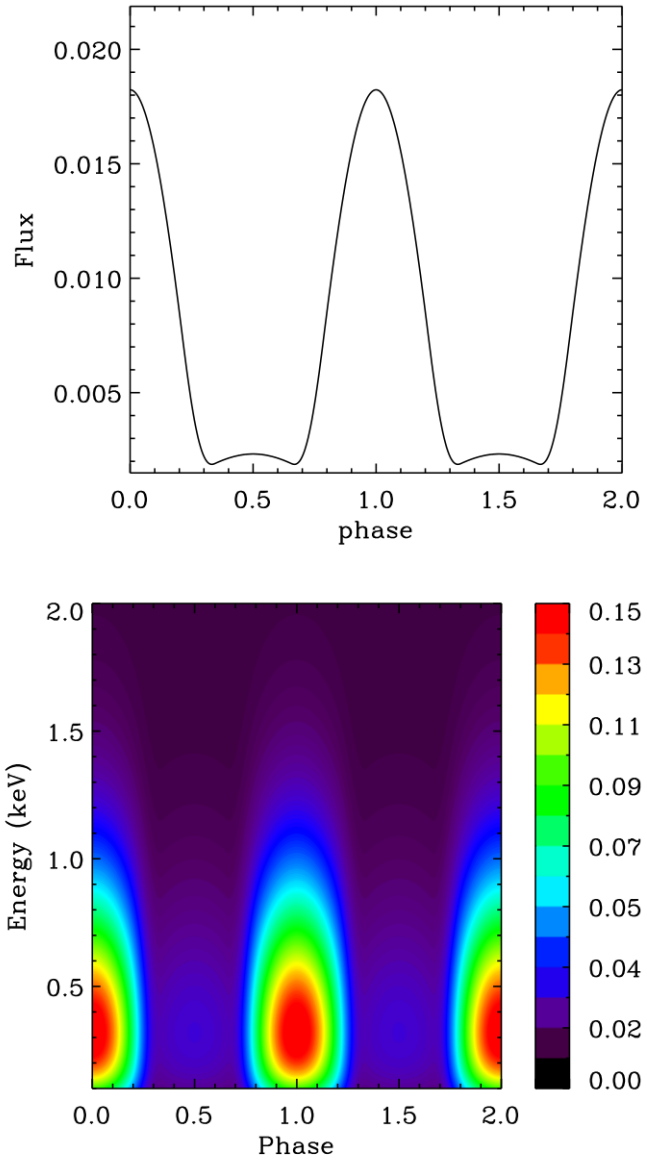

Figure 3.3: *Top*: flux as function of phase for two antipodal caps of $\theta_{c1} = 3°$ and $\theta_{c2} = 12°$. *Bottom*: countour plot of the flux as a function of the energy and the phase.

Chapter 4

Data Analysis

In this work I studied six observations for RX J2143.0+0654, six for RX J1308.6+2127, three for RX J0720.4-3125, and three for RX J1605.3+3249. The data I used come from the satellite *XMM-Newton* and are relative to the EPIC PN camera, one of the three X-ray CCD detectors carried by the *XMM-Newton* spacecraft. More details of the science instruments on board satellite are reported in Appendix A; Appendix B contains the journal of the observations used in our analysis.

All the observations are public and can be downloaded from the on line database[1].

4.1 Analysis of *XMM-Newton* data

The data analysis started by downloading the rough data from the on line XMM-Newton Science Archive. The rough data needed a first preliminary analysis, performed using the standard functions provided by Science Analysis Software (SAS) and employing the most updated calibration files. SAS is a collection of tasks, scripts and libraries, specifically designed to reduce and analyse data collected by the *XMM-Newton* observatory. The final result of this analysis is a file of events for each observation. Using then an astronomical imaging and data visualization application, I obtained an image like the two reported in figure 4.1 for each acquisition.

Once the images were obtained, the next step was to locate and to extract the source. I selected as extraction region a circle with radius of ~ 30" around the source; in order to derive the background I used a circle with radius of ~ 60" in a zone far from the source in the same CCD. For the two sources RX J1605.3+3249 and RX J0720.4-3125, the brightest among the M7 which

[1] `http://nxsa.esac.esa.int/nxsa-web/`

show an absorption feature, observations were affected by pile-up. Photon pile-up consists of the arrival of more than one X-ray photon in one camera pixel or in adjacent pixels before it is read out; the detected energy of a piled event is approximately equal to the sum of the energies of the individual photon events of which is comprised. As a consequence the detected spectral shape from the source is distorted. I selected as extraction region an annulus with inner radius of ~ 8" and outer radius of ~ 30" in order to minimise the pile-up effect, in fact with this shape I discarded the central pixels, which are the most affected by pile-up being the brightest. The background was estimated as for the other sources.

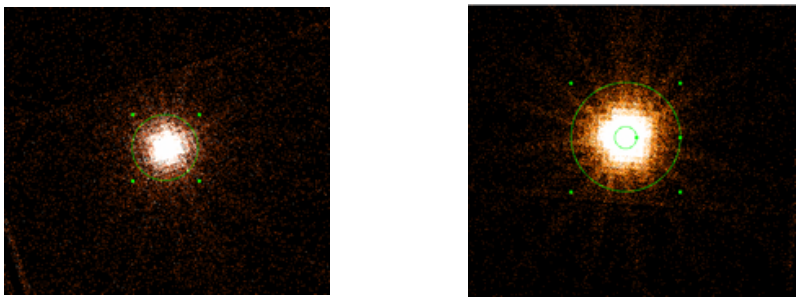

Figure 4.1: *Left*: the image of the source RX J1308.6+2127. *Right*: the image of the source RX J1605.3+3249. Both images are created using SAOImage DS9.

Using the SAS function `evselect`, photons from the selected regions are extracted. It was necessary to have a look at the event files just created, because during the observation some solar flares could occur, blinding the CCDs. For this purpose the events had to be binned using again the function `evselect`, building the light curve, which describes the trend of photon rate in function of time. Usually solar flares last even few hours, thus, in order to make them easily detectable, a 100 s bin was chosen. In figure 4.2 the left panel is the light curve of the source RX J1605.3+3249, whereas the right panel is the light curve of the all CCDs. The proof that a solar flare occurred is the presence of a sudden increase of photon rate in the second one; if the flare came from the source, an increase would have been observed also in its light curve.

To remove the time span in which the solar flare occurred, I ran the SAS tool `tabgtigen`, the purpose of which is to produce Good Time Intervals for data processing. Indeed it selected only the events that are characterized by a rate lower than an appropriate threshold. Once all the solar flares were removed, I could extract the spectra from the event files using again the

function `evselect`.

In addition to the calibrated products coming from the `evselect`, the spectra analysis requires information about the characteristics of the instrument; this information is known as the EPIC detector response and is useful to simulate an output spectrum observed by EPIC. The response is proportional to the probability that an incoming photon of energy E will be detected in a channel. As such, the response is a continuous function of E. This continuous function is converted to a discrete function by the production of response matrices which define the energy ranges. The response matrices are called Redistribution Matrix File (RMF) and Ancillary Response File (ARF). The functions I used to calculate these files are `rmfgen` and `arfgen`, provided by SAS. The generated response matrices include the effective area of the telescopes together with the diffraction efficiency of the gratings, the transmission of the filters and the quantum efficiency of the detectors.

Since I chose a different size for the background extraction regions, I had to run the function `backscale` on the background spectra in order to normalize the areas of the regions. Finally for each observation I had four files: the source and the background spectra, and two response matrices. I grouped them all in one file using the specific command `grppha`. It was necessary to rebin spectra to a minimum number of counts per bin; `grppha` does not actually add together channels, but it sets a flag which is read by *Xspec* and causes *Xspec* to sum the appropriate channels (see 4.1.1). Since I use the χ^2 distribution to verify the goodness of my fits, I needed a normal statistics and at least 25 counts for each bin. After this procedure, applied to all acquisitions, the data were ready to perform spectral fitting.

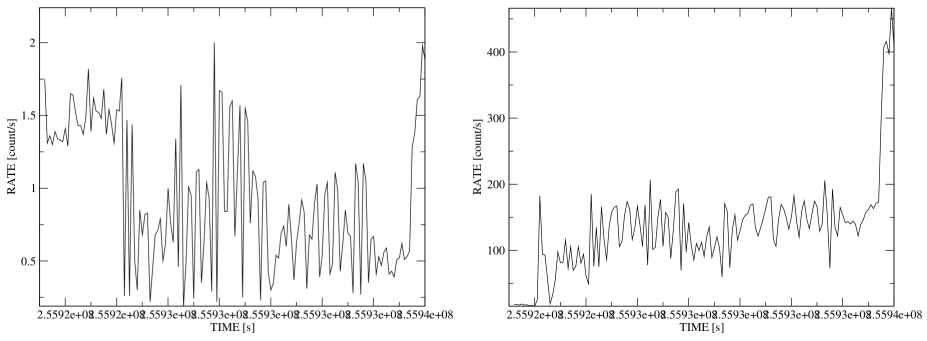

Figure 4.2: *Left*: the image of the light curve of RX J1308.6+2127. *Right*: the image of the light curve of the all CCDs for the same acquisition; a solar flare can be observed.

4.1.1 Spectral fitting

To analyse the spectra I used the program *Xspec* (version 12.8), a command-driven, interactive, X-ray spectral fitting program designed to be completely detector-independent and provided by NASA. *Xspec* allows the construction of composite models consisting of additive components representing different X-ray emission models (e.g. power-laws, blackbody), and multiplicative components, which modify the former by an energy dependent factor (e.g. photoelectric absorption, edges). The model spectrum is calculated using the energy ranges defined by the user and is in units of photons $\mathrm{cm}^{-2}\ \mathrm{s}^{-1}\ \mathrm{keV}^{-1}$.

In order to take into account interactions between photons and interstellar medium (ISM), I needed to convolve the model spectrum with a photoelectric absorption function (PA). The absorption depends on the energy of the emitted photons; low energy photons have a large photoelectric cross section. In the analysis I used two models of PA:

1. `phabs` model with Anders and Grevesse solar abundances [49] and Balucinska-Church and McCammon photoelectric cross sections [50]. Its equation is
$$M(E) = \exp[-N_H \sigma(E)], \tag{4.1}$$
where $\sigma(E)$ is the photoelectric cross section (not including Thomson scattering) and N_H is the equivalent hydrogen column in units of 10^{22} atoms cm^{-2};

2. `tbabs` model, which calculates the cross section for X-ray absorption by the ISM as the sum of the cross sections due to the gas-phase ISM, the grain-phase ISM, and the molecules in the ISM. The ISM abundances can be found in [51]; abundances are set to zero for those elements which are not included in the paper. This model allows the user to vary just the molecular hydrogen column N_H.

Since the sources I studied are nearby objects, they suffer little interstellar absorption, $N_H \sim 10^{20}\ \mathrm{cm}^{-2}$, as shown in table 3.2.

I used the blackbody model `bbodyrad` (BB) with normalization proportional to the surface area to model the source. The equation to which it refers is
$$A(E) = \frac{K \times 1.0344 \times 10^{-3} E^2}{\exp\left(\frac{E}{KT}\right) - 1} dE, \tag{4.2}$$
which introduces two parameters: the temperature kT in keV and the nor-

malization K. The factor K is equal to

$$K = \frac{R_{km}^2}{D_{10}^2}, \tag{4.3}$$

where R_{km} is the source radius in km and D_{10} is the distance to the source in units of 10 kpc; from K it is possible to determine the dimension of the emitting region if the distance is known.

I fitted the absorption feature with two models which describe a Gaussian line profile:

1. `gabs` is a multiplicative model with equation

$$M(E) = \exp\left(- \frac{par3}{\sqrt{2\pi}\sigma} \exp\left(- 0.5\left(\frac{E - E_0}{\sigma}\right)^2\right)\right), \tag{4.4}$$

   where E_0 is the line energy in keV, σ is line width in keV, and $par3$ is the line depth;

2. `gaussian` is an additive model; its equation is

$$M(E) = K\frac{1}{\sigma\sqrt{2\pi}} \exp\left(- \frac{(E - E_0)^2}{2\sigma}\right), \tag{4.5}$$

   where E_0 and σ are the line energy and width in keV, and K is the area subtended by the curve in units of photons cm^{-2} s^{-1}.

The model with which I fitted all the observations was a convolution of a PA with a BB, with the addition of a line model, for instance `phabs*gabs*bbodyrad` or `phabs*(bbodyrad+gaussian)`.

4.2 Results

My analysis can be divided in two steps.

First of all, I proceeded to the spectral analysis in the standard way. For each source I fitted all the available spectra simultaneously, because the observed flux was stable between all the observations; as a consequence I tied all the model parameters within them. The absorption from the ISM has to be the same for all acquisitions which refer to the same neutron star, thus I tied the value of N_H within the different observations. In this way the hydrogen absorption introduced just one parameter to the fit of a set of spectra. I used a BB+line model with Gaussian width σ fixed to a given value, $\sigma = 0.1$ keV.

Freezing σ is a standard way to proceed in fitting observations, when broad, weak features are present (see, e.g., [52]). I performed this analysis in order to obtains the absorption feature energies from data at my disposal. The values which I estimated are slightly different from those found in literature (table 3.2), because I used less observations.

The second part of my work consists of building temperature profiles in order to create new models with which I fit spectra. I wanted to compare the χ^2_ν (χ^2 normalized by the number of degrees of freedom, dof) values obtained from the previous fits with those got by these new models. I explored a variety of inhomogeneous surface temperature distributions without discussing their physical origin, indeed these profiles do not take into account the contributions of the magnetic field strength, the crustal temperature and the internal composition of the star.

To build these profiles I needed to set the temperature, which could be constant or show a dependence on angle θ, and semi-aperture of the caps (see 3.3). A fit with two blackbody components can give hints in order to obtain this information. It is necessary to point out that a two BB fit is not the correct model for these sources, indeed I obtained unacceptable χ^2_ν values, but I used it as a starting point. Thanks to these fits I could verify the presence of a hot spot and an estimate of the emitting region dimension could be obtained from the ratio of the normalization factors K. This procedure was applied to two sources, whereas for the other two XDINSs the two BB fit did not converge or the two components had the same temperature. In the former case I investigated the possibility of a thermal map made of one or two hot spots at constant temperature T_1 while the rest at constant temperature T_2. I specify these models are different from considering the sum of two blackbody components which cover all the star surface. In the latter case I created profiles which considered a constant temperature on the spots while a temperature $T(\theta)$ on the rest or a $T(\theta)$ on both. Then I applied these models, which show a dependence on angle, also to the former sources changing certainly the parameters.

Once chosen the parameters, I ran the program to calculate the phase-averaged spectra. Thanks to the function `flx2tab` the output text file could be converted to an *Xspec* model which was imported into the spectral fitting package with the command `atable`. Then I simulated observed spectra using the response matrices in the `fakeit` procedure; for each model, I fixed the exposure time to be long enough to obtain a number of photons that would allow to detect possible spectral features. I fitted each simulated spectra with a BB+line model in order to verify the presence of an absorption features

with similar parameters of the observed ones. If it was present, I fitted the observed spectrum with this model.

In the following paragraphs I report the results of this analysis.

4.2.1 RX J2143.0+0654

RX J2143.0+0654 was discovered as isolated neutron star in archival *ROSAT* observations by Zampieri et al. [53] in 2001. Its coordinate are RA=($21^h43^m04^s$) and Dec=(+6°54'20") (J2000).

I use six spectra considering energies between 0.2-1.3 keV. I fit them with the model `phabs*gabs*bbodyrad`; the best-fit BB+line model gives $N_H = (1.70 \pm 0.09) \times 10^{20}$ cm^{-2}, $E_0 = 779 \pm 7$ eV, $kT = 106 \pm 4$ eV, and $\chi^2_\nu = 1.05$ (figure 4.3). Uncertainties in the fit parameters represent 1σ confidence level.

I create several inhomogeneous temperature distribution profiles, of which I report only the models that provide an acceptable χ^2_ν (table 4.1):

1. model 1 consists of one hot spot with semi-aperture $\theta_c = 6.5°$ at constant temperature $T = 170$ eV, while the rest of the surface is at temperature $T = 100$ eV. This model provides a fit with $\chi^2_\nu = 1.12$ and a column density $N_H = (2.13 \pm 0.05) \times 10^{20}$ cm^{-2};

2. model 2 is made of two hot antipodal spots with $\theta_c = 6.5°$ and temperature $T = 167$ eV, whereas the temperature of the rest of the star is $T = 100$ eV. Fitting the data with this profile results in a χ^2_ν of 1.12 and N_H of $(2.22 \pm 0.05) \times 10^{20}$ cm^{-2};

3. in model 3 there is a hot spot with $\theta_c = 3°$, which follows the temperature profile $T(\theta) = 150 \times \exp(-\theta^2)$ eV; the rest of the surface has a temperature $T(\theta) = 60 \times (1 + \cos^2\theta)$ eV. The respective fit gives $\chi^2_\nu = 1.15$ and $N_H = (2.33 \pm 0.05) \times 10^{20}$ cm^{-2};

4. model 4 uses the same profiles as model 3; but there are two antipodal hot spots with semi-aperture 3°. This model fits the spectra with $\chi^2_\nu = 1.15$ and $N_H = (2.33 \pm 0.05) \times 10^{20}$ cm^{-2}.

If θ_c doubles in the latter two models, reduced chi-square does not significantly change, $\Delta\chi^2_\nu \sim 10^{-3}$.

The models I create show values of N_H higher with respect to BB+line model; reduced chi-squares are slightly higher than the χ^2_ν obtained from

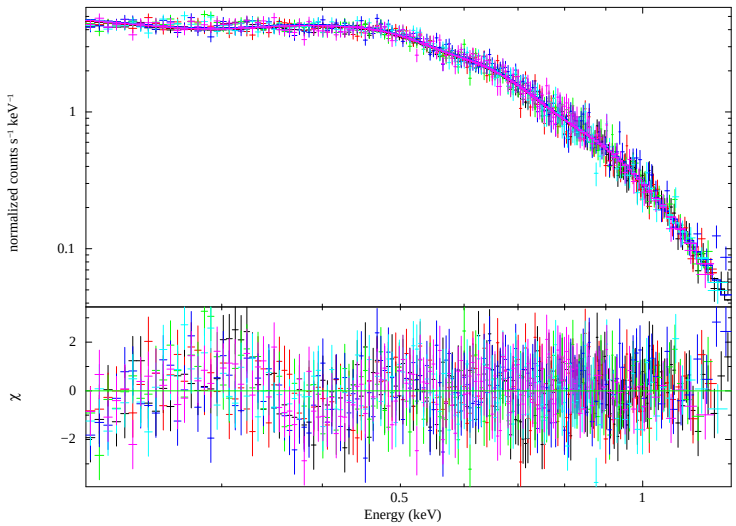

N_H (10^{20} cm^{-2})	kT eV	E_0 eV	χ^2_ν	dof
1.70 ± 0.09	106 ± 4	779 ± 7	1.05	940

Figure 4.3: *Top*: unfolded spectra of RX J2143.0+0654 and best-fit BB+line model with residuals in units of χ_ν; each observation corresponds to a color. *Bottom*: fit parameters of the best-fit BB+line model.

the best-fit BB+line model. A more refined model, such as those developed by Viganò [1] using the most updated envelope models, could improve the quality of the fit, lowering the reduced chi-square.

Model	χ^2_ν	dof	N_H (10^{20} cm^{-2})
BB+line	1.05	940	1.70 ± 0.09
model 1	1.12	945	2.13 ± 0.05
model 2	1.12	945	2.22 ± 0.05
model 3	1.15	945	2.33 ± 0.05
model 4	1.15	945	2.33 ± 0.05

Table 4.1: Summary table with values of models used for RX J2143.0+0654.

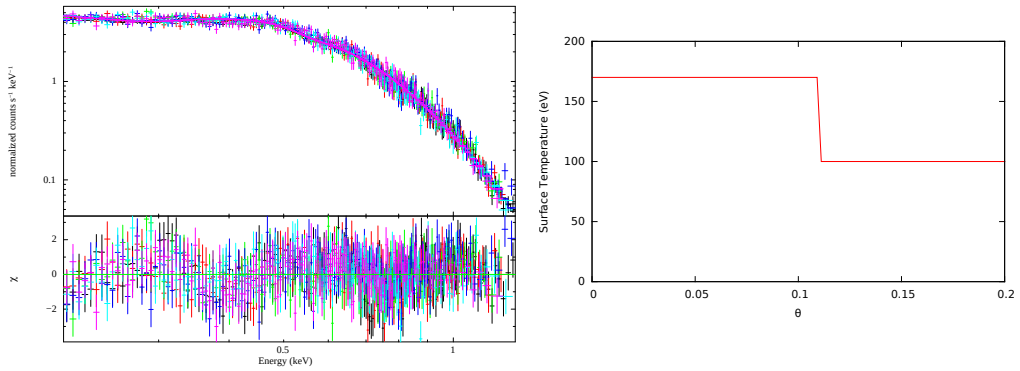

Figure 4.4: *Left*: spectra of RX J2143.0+0654 with fit provided by model 1. *Right*: temperature map of model 1.

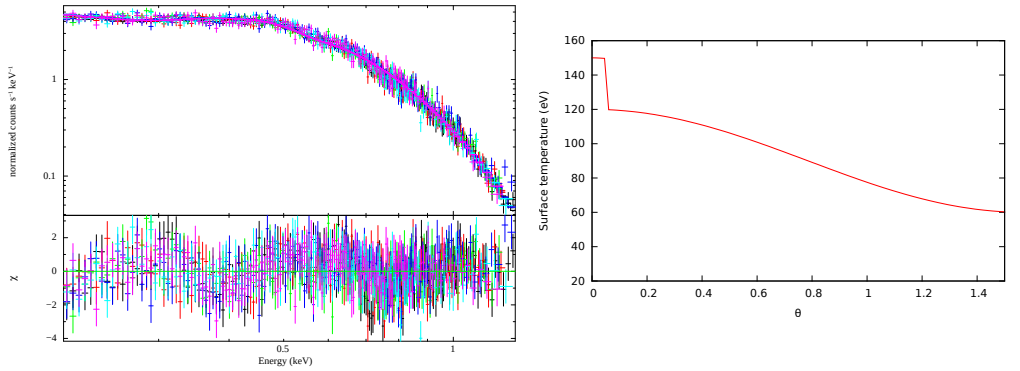

Figure 4.5: *Left*: spectra of RX J2143.0+0654 with fit provided by model 3. *Right*: temperature map of model 3.

4.2.2 RX J0720.4-3125

RX J0720.4-3125 was discovered in the *ROSAT* all-sky survey by Haberl et. al. [54] in 1997. Its coordinate are RA=($7^h20^m24^s$) and Dec=(-31°25'50") (J2000).

Among the M7, RX J0720.4-3125 is the only one which has shown long-term variations of its spectral and temporal properties. For the analysis I chose three observations in which the observed flux is stable, so I can tie all the parameters within them. I fit these spectra with the model

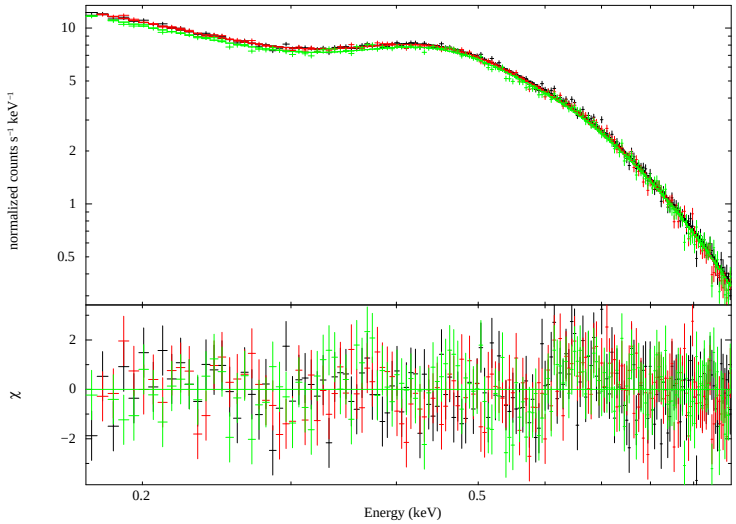

N_H (10^{20} cm^{-2})	kT eV	E_0 eV	χ^2_ν	dof
1.02 ± 0.87	102.7 ± 0.2	331 ± 2	1.18	477

Figure 4.6: *Top*: unfolded spectra of RX J0720.4-3125 and best-fit BB+line model with residuals in units of χ_ν. *Bottom*: fit parameters of the best-fit BB+line model.

`tbabs*gabs*bbodyrad` in the energy channels within 0.1 keV and 1.0 keV. The best-fit BB+line model provides $N_H = (1.02 \pm 0.87) \times 10^{20}$ cm^{-2}, $E_0 = 331 \pm 2$ eV, $kT = 102.7 \pm 0.2$ eV, and $\chi^2_\nu = 1.18$ (figure 4.6). Uncertainties in the fit parameters represent 1σ confidence level.

For this source a two BB fit does not converge, thus I have not got any suggestions of temperatures and semi-aperture of the caps. I start to build a surface temperature profile that consists of a hot spot with semi-aperture $\theta_c = 9^\circ$ at constant temperature $T = 100$ eV, while the rest of the surface follows a profile $T(\theta) = 20\times(1+\cos^2\theta)$ eV. This model is very unsatisfactory, because it provides a fit with $\chi^2_\nu = 14$ for 483 dof. In order to lower the reduced chi-square, I reduce the semi-aperture of the hot spot. I obtain the lowest χ^2_ν ($\chi^2_\nu = 8.64$ for 483 dof) with a cap of $\theta_c = 5^\circ$ and the same temperature profiles as above. The fit results of this model can be seen in table 4.2. This model provides a poor description of the spectra at low energy; I change the temperature profile of the hot spot, trying $T(\theta) = 100\times\exp(-\theta^2)$ eV or

T(θ)=100$\times\theta^{-2}$ eV, however this has no effect on the fit parameters.

For RX J0720.4-3125 I do not find an inhomogeneous surface temperature profile which can model the absorption feature.

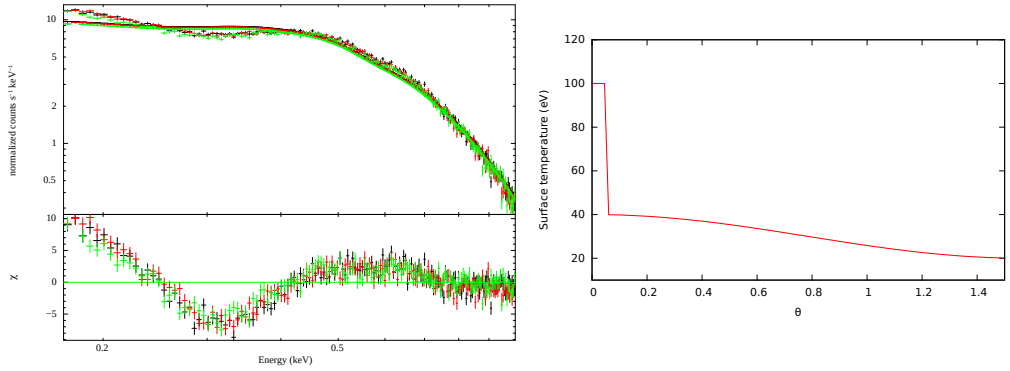

Figure 4.7: *Left*: spectra of RX J0720.4-3125 with fit provided by the model. *Right*: temperature map of the model.

Model	χ^2_ν	dof	N_H (10^{20} cm^{-2})
BB+line	1.18	477	1.02 $\pm$ 0.87
model	8.64	483	6.11 $\pm$ 0.02

Table 4.2: Summary table with values of models used for RX J0720.4-3125.

4.2.3 RX J1605.3+3249

In 1999 Motch et al. [55] discovered RX J1605.3+3249 as a nearby isolated neutron star detected from its thermal emission, analysing *ROSAT* observations. Its coordinate are RA=($16^h05^m18^s$) and Dec=(+32°49'07") (J2000).

Three spectra are used in the energy band 0.1-1 keV. Fitting the data with the model `phabs*gabs*bbodyrad` results in $N_H = (0.8 \pm 0.1) \times 10^{20}$ cm^{-2}, $E_0 = 497 \pm 3$ eV, $kT = 91.5 \pm 0.7$ eV, and $\chi^2_\nu = 1.37$ (figure 4.8). Uncertainties in the fit parameters represent 1σ confidence level.

I explore different surface temperature profiles, of which I report those that provide the lowest χ^2_ν (table 4.3) :

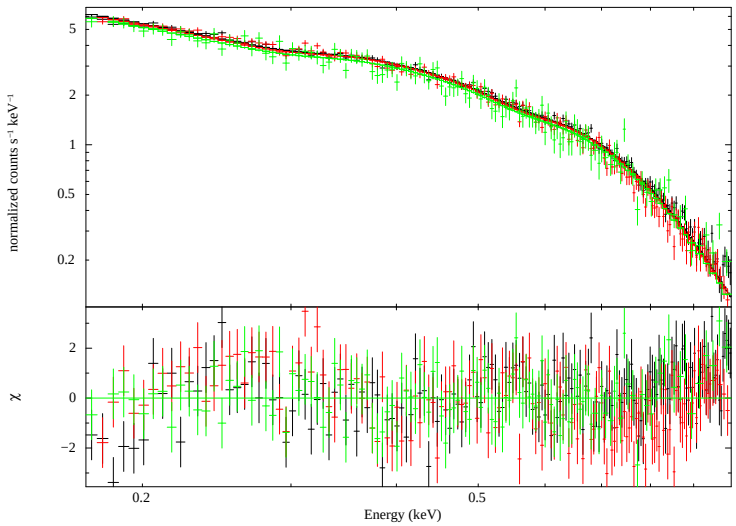

N_H (10^{20} cm^{-2})	kT eV	E_0 eV	χ^2_ν	dof
0.8 ± 0.1	91.5 ± 0.7	497 ± 3	1.4	439

Figure 4.8: *Top*: unfolded spectra of RX J1605.3+3249 and best-fit BB+line model with residuals in units of χ_ν. *Bottom*: fit parameters of the best-fit BB+line model.

1. model 1 is made of a hot spot with semi-aperture $\theta_c = 1.5°$ at constant temperature $T = 97$ eV, while the rest of the surface is at temperature 30 eV. This model fits the spectra with $\chi^2_\nu = 1.46$ and column density $N_H = (6.22 \pm 0.02) \times 10^{20}$ cm^{-2};

2. model 2 uses the same temperatures as model 1, but there are two antipodal hot spots with $\theta_c = 1.5°$. The fit results of this model are $\chi^2_\nu = 1.59$ and $N_H = (5.58 \pm 0.02) \times 10^{20}$ cm^{-2};

3. model 3 consists of a hot spot with $\theta_c = 1.5°$ which has a temperature $T(\theta) = 100 \times \exp(-\theta^2/8)$ eV, whereas the rest of the surface follows a profile $T(\theta) = 30 \times (1 + 2.8 \cos^2\theta)$ eV. This model provides a fit with $\chi^2_\nu = 2.07$ and $N_H = (0.06 \pm 0.02) \times 10^{20}$ cm^{-2};

4. in model 4 there are two antipodal hot spots with $\theta_c = 1.5°$ and the temperature profiles are the same as model 3. The fit gives $\chi^2_\nu = 2.08$ and $N_H = (0.03 \pm 0.03) \times 10^{20}$ cm^{-2}.

The first two models have reduced chi-squares slightly higher than the χ^2_ν obtained from the best-fit BB+line model. A model, which takes into account magnetic field and crustal temperature, could provide a better description of the source spectra, lowering the reduced chi-square.

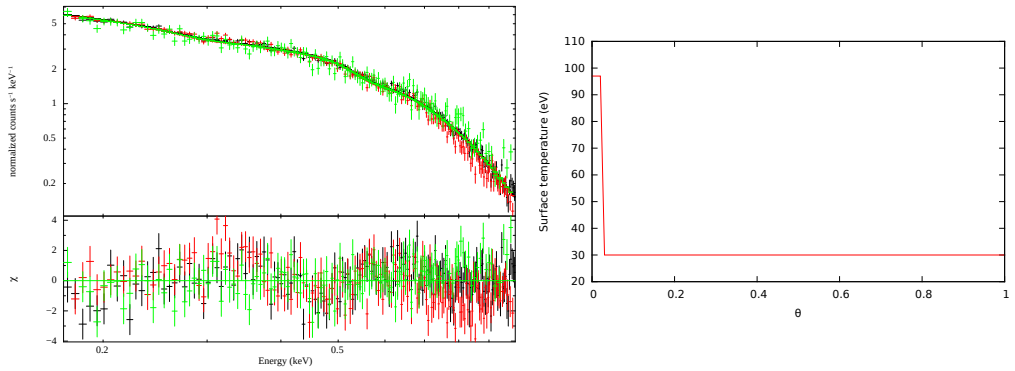

Figure 4.9: *Left*: spectra of RX J1605.3+3249 with fit provided by model 1. *Right*: temperature map of model 1.

Model	χ^2_ν	dof	N_H (10^{20} cm^{-2})
BB+line	1.37	439	0.8 ± 0.1
model 1	1.46	451	6.22 ± 0.02
model 2	1.59	451	5.58 ± 0.02
model 3	2.07	451	0.06 ± 0.02
model 4	2.08	451	0.03 ± 0.03

Table 4.3: Summary table with values of models used for RX J1605.3+3249.

4.2.4 RX J1308.6+2127

RX J1308.6+2127 was discovered by Schwope et al. [56] in 1999. Its coordinate are RA=($13^h08^m48^s$) and Dec=(+21°27'08") (J2000).

I consider six spectra in the energy channels within 0.1 keV and 1.5 keV. I choose the model `phabs*(gaussian+bbodyrad)`; the best-fit BB+line gives $N_H = (0.45 \pm 0.10) \times 10^{20}$ cm^{-2}, $E_0 = 425 \pm 5$ eV, $kT = 134 \pm 3$ eV, and $\chi^2_\nu = 1.14$ (figure 4.10). Uncertainties in the fit parameters represent 1σ

confidence level.

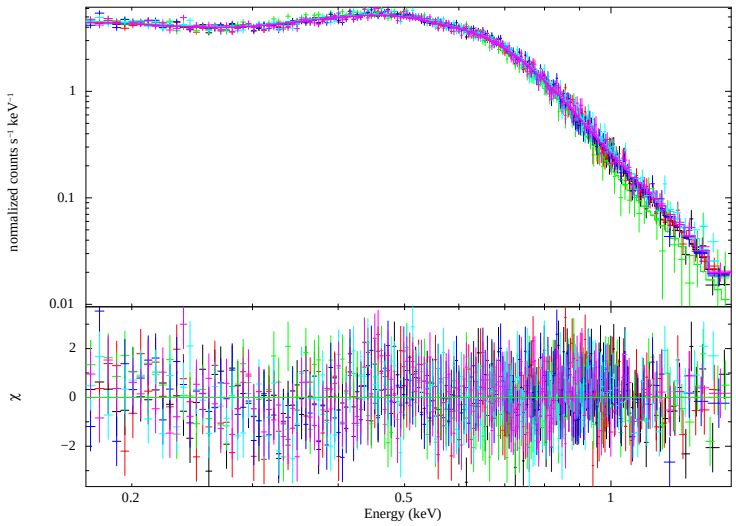

N_H (10^{20} cm^{-2})	kT eV	E_0 eV	χ^2_ν	dof
0.45 ± 0.10	134 ± 3	425 ± 5	1.14	1068

Figure 4.10: *Top*: unfolded spectra of RX J1308.6+2127 and best-fit BB+line model with residuals in units of χ_ν. *Bottom*: fit parameters of the best-fit BB+line model.

Fitting the spectra with a two BB model, the two components have the same temperature.

I built several surface temperature profiles, however I do not find a model which can provide a better description than a BB+line model. Among the models I explore, the lowest reduced chi-square I can obtain is 5.23. I report two models:

1. model 1 consists of a hot spot of $\theta_c = 10^\circ$ at constant temperature $T = 100$ eV, while the rest of the surface follows a profile $T(\theta) = 50\times(1+\cos^2\theta)$ eV. This model fits the spectra with $\chi^2_\nu = 5.23$ and $N_H = (0.10 \pm 0.05) \times 10^{20}$ cm^{-2};

2. model 2 is made of two antipodal hot spots with $\theta_c = 5^\circ$, the temperature profiles are the same as model 1. The fit parameters are $\chi^2_\nu =$

5.28 and $N_H = (0.10 \pm 0.06) \times 10^{20}$ cm^{-2}.

As shown in figure 4.11, both models exhibit a strong trend in the residuals. Among the M7 which show absorption features in the spectrum, RX J1308.6+2127 is the one with the highest equivalent width, $E_w = 150$ eV. This could be a hint to understand the origin of these features in absorption. The absorption feature in PSR J1819-1458 has an E_w of 400 eV; it should be verified if also this spectral feature can not be modelled with an inhomogeneous temperature profile.

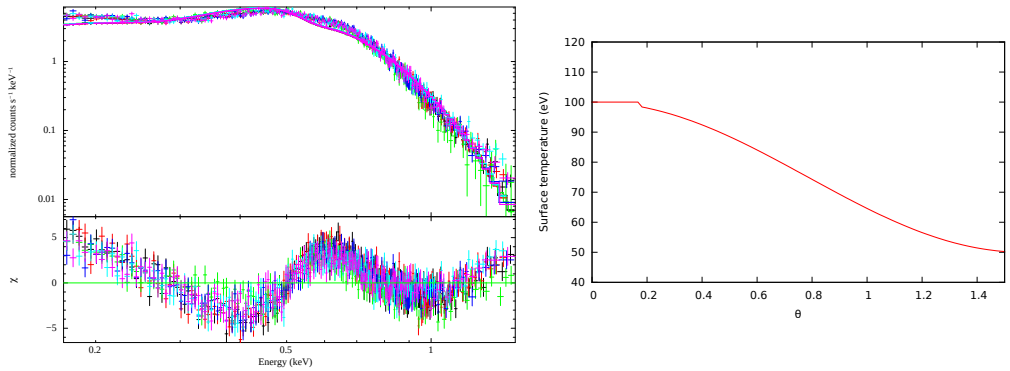

Figure 4.11: *Left*: spectra of RX J1308.6+2127 with fit provided by model 1. *Right*: temperature map of model 1.

Model	χ^2_ν	dof	N_H (10^{20} cm^{-2})
BB+line	1.14	1068	0.45 ± 0.10
model 1	5.23	1077	0.10 ± 0.05
model 2	5.28	1077	0.01 ± 0.05

Table 4.4: Summary table with values of models used for RX J1308.6+2127.

Chapter 5

Conclusions

In a small number of objects the thermal X-ray spectra show deviations from a pure blackbody in form of broad features. The origin of these absorption features is still unknown; several explanations have been suggested. They can be reproduced by proton/electron cyclotron resonances and/or by atomic transitions in magnetised atmosphere. A new interpretation has been put forward by Viganò et al. [1]. They consider the possibility that distortions from a perfect Planckian spectrum can be induced by an inhomogeneous temperature distribution on the neutron star surface. Understanding the origin of these spectral lines can help to constraint the chemical composition and the magnetic field of the star.

I investigate the nature of absorption features, focusing on the latter hypothesis. I apply the method proposed by Viganò et al. to a sample made of four XDINS: RX J2143.0+0654, RX J0720.4-3125, RX J1605.3+3249, and RX J1308.6+2127. First of all I perform the spectral fitting analysis in the standard way, thus the absorption feature energy values are estimated from the observations at my disposal. Then I build several surface temperature profiles in order to find models that improve the goodness of the fit with respect to blackbody model plus a Gaussian.

RX J0720.4-3125 and RX J1308.6+2127 are cases for which the deviations from a BB model do not appear to be reproducible by inhomogeneous temperature maps. Among the XDINSs, RX J0720.4-3125 is the only one that has shown long-term variations of its spectral properties and its feature equivalent width follows this evolution, varying from 0 to 70 eV; RX J1308.6+2127 has the highest value of the equivalent width, $E_w = 150$ eV. My surface temperature models provide fits with χ^2_ν which exceeds the BB+line model χ^2_ν of 4 units for RX J1308.6+2127 and 7 units for RX J0720.4-3125.

For the other two sources, RX J2143.0+0654 and RX J1605.3+3249, I find surface temperature distributions able to give acceptable fits which have slightly higher χ^2_ν than the BB+line model, $\Delta\chi^2_\nu = 0.09$. At least for these objects, the temperature anisotropy can reproduce absorption features similar to the observed ones. However, my models do not take into account magnetic field strength, internal neutron star composition and crustal temperature, thus a more refined model can significantly improve the quality of the fit, lowering the reduced chi-squared.

In general, given the wide space of parameters of the temperature modelling, reconstructing the surface temperature map is a highly degenerate problem. Thanks to Viganò's work and this thesis it is demonstrated that the contribution to absorption features from inhomogeneous temperature distributions can be significant and this should be accounted for in combination with more sophisticated emission models.

Next steps consist of computing the predicted pulsed fraction and light curves for each model and comparing them with source data. Moreover models, in which the geometrical angles χ and ξ become parameters, will be developed.

Appendix A

XMM-Newton

The data I analysed during this work are from the satellite X-Ray Multi-mirror Mission, also called *XMM-Newton*. In this section the instrumentations on board of this satellite are described.

XMM-Newton is an ESA satellite, launched on December 10^{th}, 1999 and carries two distinct types of telescope: three Wolter type-1 X-ray telescopes[1], with different X-ray detectors in their foci, and a 30-cm optical/UV telescope with a microchannel-plate pre-amplified CCD detector in its focal plane. Thus, it is possible to explore simultaneously at X-ray and optical/UV wavelengths. It provides three types of science instrument:

1. European Photon Imaging Camera (EPIC): three CCD cameras of two different types, MOS and PN, for X-ray imaging, spectroscopy and photometry;

2. Reflection Grating Spectrometer (RGS): two spectrometers for high-resolution X-ray spectroscopy and spectro-photometry;

3. Optical Monitor (OM) for optical/UV imaging.

They are six instruments, which can operate simultaneously or independently and each in different modes of data acquisition.

The Wolter telescopes consist of 58 thin nested mirror shells that achieve good angular resolution quantifiable with a point-spread function (PSF) with

[1] A Walter telescope consists of co-axial and con-focal paraboloidal and hyperboloidal mirrors. X-rays are first reflected by an internally reflecting paraboloidal mirror and then reflected to the prime focus of the telescope bt the internally reflecting hyperboloidal mirror.

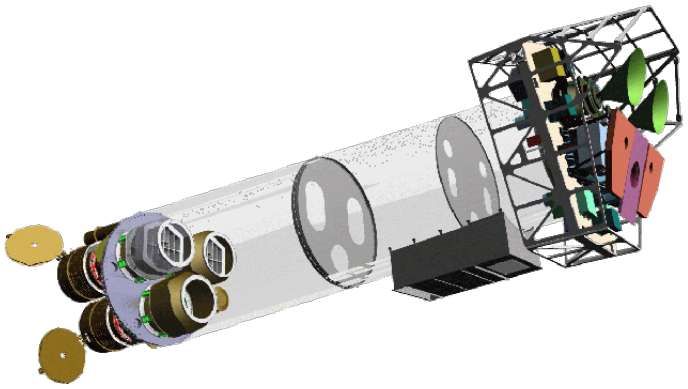

Figure A.1: Sketch of the *XMM-Newton* payload. The mirror modules, two of which are equipped with Reflection Grating Arrays, are visible at the lower left. At the right end of the assembly, the focal X-ray instruments are shown: the EPIC MOS cameras with their radiators (black/green horns), the radiator of the EPIC PN camera (violet) and those of the (light blue) RGS detectors (in pink). The OM telescope is obscured by the lower mirror module. Figure courtesy of Dornier Satellitensysteme GmbH.

a full width at half maximum (FWHM) on the order of 6". *XMM-Newton* carries the X-ray telescopes with the largest effective area of a focusing telescope ever: the total mirror geometric effective area at 1.5 keV is $\sim$ 1550 cm^2 for each telescope. The EPIC CCD cameras have moderate spectral resolution with a resolving power $E/\Delta E \sim$ 20-50, while the RGS spectrometers offer much higher spectral resolution, with a resolving power in the range of 200-800. A highly elliptical orbit offers continuous target visibility of up to about 40 hours; this is very favourable for studies of source variability and also in order to achieve a high overall observatory efficiency.

The quality of an X-ray mirror modulo is its ability to focus photons; this can estimate by the PSF which describes the response of an imaging system to a point source. Each telescope on board *XMM-Newton* has its own PSF.

Since in this work I only use data coming from EPIC PN camera, I describe briefly its properties, omitting all the other scientific devices.

The *XMM-Newton* EPIC cameras offer the possibility to perform extremely sensitive imaging observations over a field of view of 30' and in the energy range from 0.15 to 12 keV, with moderate spectral ($E/\Delta E \sim$ 20-50)

and angular resolution ($\sim$ 6" FWHM).

The heart of the PN camera is a single Silicon wafer with 12 CCD integrated chips. There are four individual quadrants, each of which has three PN-CCD subunits with a format 200 $\times$ 64 pixels; they are operated on parallel. The imaging area is 6 $\times$ 6 cm, covering about 97% of the field of view, and the pixel size is 150 $\times$ 150 μm (4.1 arcsec) with a position resolution of 120 μm. The readout of the PN chips is much faster than that of the MOS cameras, because each pixel column has its own readout node. Another important difference is that the MOS chips are front-illuminated, while the PN CCDs are back-illuminated, which affects the detector quantum efficiencies decisively. The PN chip array is slightly offset with respect to the optical axis of its X-ray telescope so that the nominal, on-axis observing position does not fall on the central chip boundary. This ensures that $\geq$ 90% of the energy of an on-axis point source are collected on one PN CCD chip. The PN type camera can be operated with very high time resolution down to 0.03 ms in the timing mode and 0.007 ms in the burst mode.

The EPIC background can be classified into two contributions: a cosmic X-ray background and an instrumental background. The latter component may be further divided into a detector noise component, which becomes important at low energies (below 200 eV) and a second component which is due to the interaction of particles with the structure surrounding the detectors and the detectors themselves. This component is characterized by a flat spectrum and is particularly important at high energies (above a few keV).

The particle induced background can be divided into 2 components: an external 'flaring' component, characterized by strong and rapid variability, which is often totally absent, and a second more stable internal component. The flaring component is currently attributed to soft protons with energies smaller than a few 100 keV, which are presumably funneled towards the detectors by the X-ray mirrors. The stable component is due to the interaction of high-energy particles, with energies larger than some 100 MeV, with the structure surrounding the detectors and possibly the detectors themselves.

Appendix B

Observation specifications

I report the journal of the *XMM-Newton* observations used in the data analysis.

RX J0720.4-3125

	Obs. ID	Start date	End date	Duration [s]
1	0300520201	2005-04-28 08:41:05	2005-04-28 23:29:35	53310
2	0300520301	2005-09-22 23:44:23	2005-09-23 14:27:54	53011
3	0164560501	2004-05-22 10:15:22	2004-05-23 00:41:13	51951

Table B.1: Observation specifications for RX J0720.4-3125.

RX J1605.3+3249

	Obs. ID	Start date	End date	Duration [s]
1	0671620101	2012-03-06 11:05:30	2012-03-07 03:52:28	60418
2	0157360401	2003-01-17 21:33:00	2003-01-18 09:08:17	41717
3	0302140501	2006-02-12 00:35:22	2006-02-12 05:21:17	17155

Table B.2: Observation specifications for RX J1605.3+3249.

RX J1308.6+2127

	Obs. ID	Start date	End date	Duration [s]
1	0163560101	2003-12-30 06:36:04	2003-12-30 15:31:18	32114
2	0157360101	2003-01-01 06:13:13	2003-01-01 14:15:03	28910
3	0090010101	2001-12-31 03:03:07	2001-12-31 08:42:26	20359
4	0305900601	2006-01-10 18:37:22	2006-01-10 23:18:07	16845
5	0305900201	2005-06-25 00:22:04	2005-06-25 05:02:10	16806
6	0305900401	2005-07-15 07:51:59	2005-07-15 11:58:53	14814

Table B.3: Observation specifications for RX J1308.6+2127.

RX J2143.0+0654

	Obs. ID	Start date	End date	Duration [s]
1	0201150101	2004-05-31 15:27:48	2004-05-31 23:55:17	30449
2	0502040701	2007-05-17 20:56:55	2007-05-18 00:40:24	13409
3	0502040601	2007-05-13 16:27:08	2007-05-13 20:08:47	13299
4	0502041501	2008-05-03 03:07:58	2008-05-03 06:26:33	11915
5	0502041101	2007-11-07 04:16:04	2007-11-07 07:29:13	11589
6	0502041201	2007-11-08 03:41:28	2007-11-08 06:26:46	9918

Table B.4: Observation specifications for RX J2143.0+0654.

Acknowledgements

Desidero ringraziare il Professor Roberto Turolla per avermi "iniziato" all'Astrofisica degli oggetti compatti, per aver accettato di essere il mio relatore, per le numerose ore dedicate alla mia tesi anche durante il periodo estivo e per avermi incoraggiato nelle domande di dottorato.

Ringrazio sentitamente il Dott. Daniele Viganò e la Dott.ssa Nanda Rea per avermi seguito durante il mio soggiorno all'Institut de Ciències de l'Espai di Barcellona, per essere stati molto pazienti e per avermi dato preziosi e indispensabili consigli durante la produzione di questo lavoro.

Ringrazio mamma Saveria e Elena, che mi hanno supportato e sopportato soprattutto in questa lunga calda estate, per avermi sempre incoraggiato anche quando non avevo più la forza: "Io non mollo, io ci riuscirò!".

Un grazie particolare alla "Monte Solaro Mansion" con i suoi conquilini passati, temporanei e presenti che ormai non sono solo coinquilini o compagni di corso, ma amici: ad Alessandro per tutte le cene preparate, a Carlo per le risate con Nicolas Cage, a Laura per il primo kebab mangiato, ad Alessio per la continua consulenza di questa tesi, a Cappe per avermi suggerito 'weakly', a Luca per i vari momenti (aperitivi/gelati) di pausa, a Davide per le parole di conforto sempre pronte, a Max per l'allegria che porta in giro, a Damiano e ad Andrea per avermi regalato un fine settimana di svago in un periodo di stress!

Bibliography

[1] D. Viganò et al. Spectral features in isolated neutron stars induced by inhomogeneous surface temperatures. *MNRAS*, 443:31, 2014.

[2] W. Baade; F. Zwicky. Supernovae and cosmic rays. *Physical Review*, 45:138, 1934.

[3] A. Hewish; S. J. Bell et al. Observation of a rapidly pulsating radio source. *Nature*, 45:709, 1968.

[4] T. Gold. Rotating neutron stars as the origin of the pulsating radio sources. *Nature*, 218:731, 1968.

[5] F. Pacini. Energy emission from neutron stars. *Nature*, 216:567, 1967.

[6] J. M. Lattimer et al. The physics of neutron stars. *Science*, 304:536, 2004.

[7] C. J. Pethick. Cooling of neutron stars. *Reviews of modern physics*, 64:1133, 1992.

[8] S. Guillot et al. Neutron star radius measurement with the quiescent low-mass X-ray binary U24 in NGC 6397. *Astrophysical Journal*, 732:88, 2011.

[9] C. E. Rhoades and R. Ruffini. Maximum mass of a neutron star. *Physical Review letters*, 32:324, 1974.

[10] R. N. Manchester and J. H. Taylor. *Pulsars*. W. H. Freeman and Company, 1977.

[11] D. G. Ravenhall et al. Structure of matter below nuclear saturation density. *Physical Review letters*, 50:2066, 1983.

[12] V. I. Kondratiev et al. New limits on radio emission from X-ray dim isolated neutron stars. *Astrophysical Journal*, 702:692, 2009.

[13] P. Goldreich and W. H. Julian. Pulsar electrodynamics. *Astrophysical Journal*, 157:869, 1969.

[14] A. K. Harding. The neutron star zoo. *Frontiers of physics*, 8:679, 2013.

[15] M. A. McLaughlin et al. Transient radio bursts from rotating neutron stars. *Nature*, 438:817, 2006.

[16] T. L. Cline et al. Detection of a fast, intense and unusual gamma-ray transient. *Astrophysical Journal*, 237:L1, 1980.

[17] R. C. Duncan and C. Thompson. Formation of very strongly mangnetizec neutron stars. *Astrophysical Journal*, 392:L9, 1992.

[18] Wynn C. G. Ho. Central compact objects and their magnetic fields. *Proceedings of the International Astronomical Union*, 8:101, 2012.

[19] T. Regimbau and J. de Freitas Pacheco. Population synthesis of pulsars: magnetic field effects. *Astronomy and Astrophysics*, 374:182, 2001.

[20] P. Gonthier et al. Role of beam geometry in population statistics and pulse profiles of radio and gamma-ray pulsars. *Astrophysical Journal*, 604:775, 2004.

[21] A. Reisenegger. Magnetic fields of neutron stars. *arXiv: 0307133*, 2013.

[22] A. Reisenegger. Origin and evolution of neutron star magnetic fields. *arXiv: 0307133*, 2003.

[23] K. S. Thorne. The relativistic equations of stellar structure and evolution. *Astrophysical Journal*, 212:825, 1977.

[24] G. Glen and P. Sutherland. On the cooling of neutron stars. *Astrophysical Journal*, 239:671, 1980.

[25] F. Özel. Surface emission from neutron stars and implications for the physics of their interiors. *Reports on Progress in Physics*, 76, 2013.

[26] D. N. Aguilera et al. 2D cooling of magnetized neutron stars. *Astronomy and Astrophysics*, 486:255, 2008.

[27] J. A. Pons and U. Geppert. Magnetic field dissipation in neutron star crusts: from magnetars to isolated neutron stars. *Astronomy and Astrophysics*, 470:303, 2007.

[28] J. A. Pons et al. Magneto-thermal evolution of neutron stars. *Astronomy and Astrophysics*, 496:207, 2009.

[29] D. Viganò et al. Unifying the observational diversity of isolated neutron stars via magneto-thermal evolution models. *MNRAS*, 434:123, 2013.

[30] D. L. Kaplan et al. The parallax and proper motion of RX J1856.5–3754 revisited. *Astrophysical Journal*, 571:447, 2002.

[31] N. Sartore et al. Spectral monitoring of RX J1856.5-3754 with XMM-Newton. Analysis of EPIC-pn data. *Astronomy and Astrophysics*, 541:A66, 2012.

[32] V. Burwitz et al. The thermal radiation of the isolated neutron star RX J1856.5-3754 observed with Chandra and XMM-Newton. *Astronomy and Astrophysics*, 399:1109, 2003.

[33] M. A. McLaughlin et al. PSR J1847-0130: A radio pulsar with magnetar spin characteristics. *Astrophysical Journal*, 591:L135, 2003.

[34] M. M. Hohle et al. The continued spectral and temporal evolution of RX J0720.4-3125. *MNRAS*, 423:1194, 2012.

[35] D. L. Kaplan et al. New optical/ultraviolet counterparts and the spectral energy distributions of nearby, thermally emitting, isolated neutron stars. *Astrophysical Journal*, 736:117, 2011.

[36] H. Tong et al. The optical/UV excess of isolated neutron stars in the RCS model. *Research in Astronomy and Astrophysics*, 11:1371, 2011.

[37] R. Turolla S. Zane and J.J. Drake. Is RX J1856.5-3754 a naked neutron star ? *Advances in Space Research*, 33:531, 2004.

[38] B. Posselt et al. The magnificent seven in the dusty prairie. *Astrophysics and Space Science*, 308:171, 2007.

[39] V. I. Kondratiev et al. A search for pulsed and bursty radio emission from X[U+2010]ray dim isolated neutron stars. *AIP Conference Proceedings*, 983:348, 2008.

[40] D. L. Kaplan and M. H. van Kerkwijk. A coherent timing solution for the nearby, thermally emitting isolated neutron star RX J0420.0-5022. *Astrophysical Journal*, 740:L30+, 2011.

[41] D. Sanwai et al. Discovery of absorption features in the X-ray spectrum of an isolated neutron star. *Astrophysical Journal*, 574:L61, 2002.

[42] O. Kargaltsev et al. Absorption features in the X-ray spectrum of an ordinary radio pulsar. *Science*, 337:946, 2012.

[43] A. Camero-Arranz et al. The extended X-ray emission around RRAT J1819-1458. *MNRAS*, 429:2493, 2013.

[44] A. Tiendo et al. A variable absorption feature in the x-ray spectrum of a magnetar. *Nature*, 500:312, 2013.

[45] M. H. van Kerkwijk and D. L. Kaplan. Isolated neutron stars: Magnetic fields, distances, and spectra. *Astrophysics and Space Science*, 308:191, 2007.

[46] M. H. van Kerkwijk et al. A strong, broad absorption feature in the X-ray spectrum of the nearby neutron star RX J1605.3+3249. *Astrophysical Journal*, 608:432, 2004.

[47] R. Turolla and L. Nobili. Pulse profiles from thermally emitting neutron stars. *Astrophysical Journal*, 768:147, 2013.

[48] A. M. Beloborodov. Gravitational bending of light near compact objects. *Astrophysical Journal*, 566:L85, 2002.

[49] E. Anders and N. Grevesse. Abundances of the elements - meteoritic and solar. *Geochimica et Cosmochimica Acta*, 53:197, 1989.

[50] M. Balucinska-Church and D. McCammon. Photoelectric absorption cross sections with variable abundances. *Astrophysical Journal*, 400:699, 1992.

[51] A. Allen J. Wilms and R. McCray. On the absorption of X-rays in the interstellar medium. *Astrophysical Journal*, 542:614, 2000.

[52] F. Haberl et al. The isolated neutron star X-ray pulsars RX J0420.0-5022 and RX J0806.4-4123: New X-ray and optical observations. *Astronomy and Astrophysics*, 424:635, 2004.

[53] L. Zampieri et al. 1RXS J214303.7+065419/RBS 1774: A new isolated neutron star candidate. *Astronomy and Astrophysics*, 378:L5, 2001.

[54] F. Haberl et al. RX J0720.4-3125: strong evidence for an isolated pulsating neutron star. *Astronomy and Astrophysics*, 326:662, 1997.

[55] C. Motch et al. The isolated neutron star candidate RX J1605.3+3249. *Astronomy and Astrophysics*, 351:177, 1999.

[56] A. D. Schwope et al. The isolated neutron star candidate RBS1223 (1RXS J130848.6+212708). *Astronomy and Astrophysics*, 341:L51, 1999.